

Stochastic Triangular Mesh Mapping

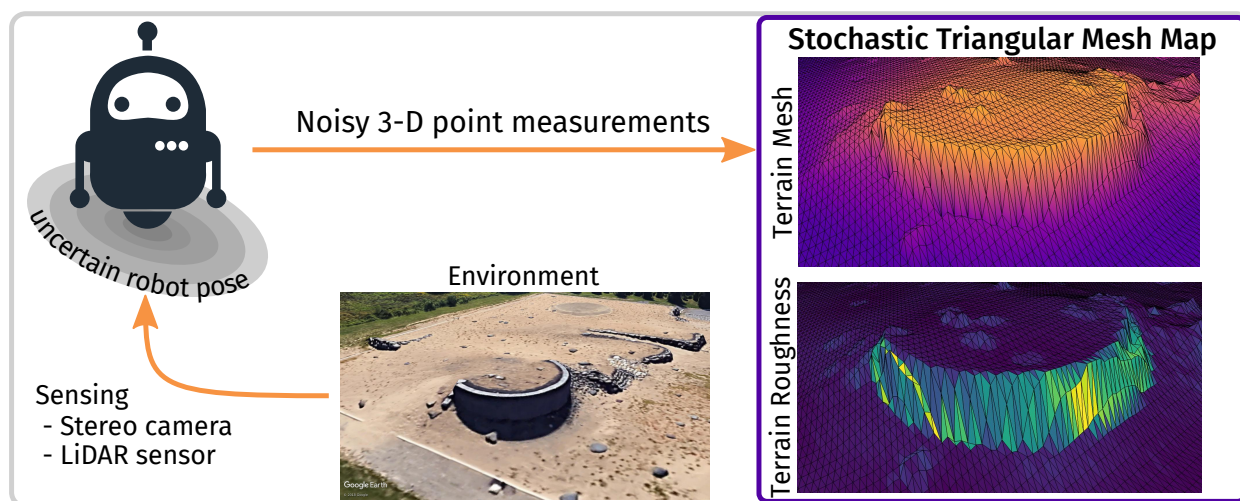
Clint D. Lombard^{a,*}, Corné E. van Daalen^a

^a*Department of Electrical and Electronic Engineering, Stellenbosch University, Stellenbosch, South Africa*

Abstract

For mobile robots to operate autonomously in general environments, perception is required in the form of a dense metric map. For this purpose, we present the stochastic triangular mesh (STM) mapping technique: a 2.5-D representation of the surface of the environment using a continuous mesh of triangular surface elements, where each surface element models the mean plane and roughness of the underlying surface. In contrast to existing mapping techniques, a STM map models the structure of the environment by ensuring a continuous model, while also being able to be incrementally updated with linear computational cost in the number of measurements. We reduce the effect of uncertainty in the robot pose (position and orientation) by using landmark-relative submaps. The uncertainty in the measurements and robot pose are accounted for by the use of Bayesian inference techniques during the map update. We demonstrate that a STM map can be used with sensors that generate point measurements, such as light detection and ranging (LiDAR) sensors and stereo cameras. We show that a STM map is a more accurate model than the only comparable online surface mapping technique—a standard elevation map—and we also provide qualitative results on practical datasets.

Graphical Abstract



Keywords: dense mapping, submapping, perception, triangular mesh, probabilistic graphical model, stereo cameras, LiDAR

*Corresponding author

Email addresses: clint dot lom at gmail dot com (Clint D. Lombard), cvdaalen at sun dot ac dot za (Corné E. van Daalen)

1. Introduction

For an autonomous mobile robot to operate effectively, it needs the ability to perceive its environment; this problem of perception is commonly referred to as *mapping*. More precisely, mapping can be defined as representing a robot’s belief over the environment, where “belief” refers to the knowledge about a state, given all measurements and any prior information. In the general case of a robot operating in an initially unknown environment, the map needs to be incrementally built online using the robot’s measurements of the environment. These measurements are obtained using exteroceptive sensors—typically a combination of light detection and ranging (LiDAR) sensors, stereo cameras, and depth-cameras. In order to perform complex tasks—such as path planning, collision detection, or object manipulation—a 3-D dense metric map is required. Guizilini and Ramos [1] argued that for a dense metric map to be an effective representation, it should have the following attributes:

- *Reason under uncertainty.* Measurements from all robot sensors contain some degree of uncertainty, which needs to be accounted for when updating the map.
- *Incremental updates.* Due to the online nature of the problem, all the measurements are not available at once, and as the robot needs to continuously query the map, the map needs to be updated incrementally.
- *Update and query efficiently.* Exteroceptive sensors generate vast amounts of data—typically in the form of dense point clouds—which needs to be quickly incorporated with the map. Additionally, the resulting map needs to be accessed quickly when required.
- *Represent the structure in the environment.* The environment is inherently structured due to spatial relationships on various length scales. By exploiting this structure, a map can interpolate in occluded regions, or better estimate regions with few measurements.

In this paper we present stochastic triangular mesh (STM) mapping, an online dense mapping technique designed around these four attributes. In particular, we focus on two aspects:

Robot pose belief. A source of uncertainty influencing dense mapping is *localisation*—determining the robot pose (position and orientation) within the environment. Therefore, to build an accurate model of the environment, one must also consider the belief over the robot pose. Estimating the robot pose belief is typically performed using the process of simultaneous localisation and mapping (SLAM), whereby the belief over a sparse map—consisting of re-identifiable landmarks—in conjunction with the robot pose is estimated. The sparsity of this landmark map, however, prohibits its use for complex planning tasks, and should rather be considered as a localisation aid. When performing SLAM, the beliefs over the robot pose at any time-step can change due to new information, as is the case when loop closure is performed. This can cause significant changes to the beliefs over these previous poses, which presents a problem as measurements obtained at previous poses would have been incorporated into the dense map using the previous pose beliefs. To account for this, measurements would need to be removed and reintegrated into the map using the retroactively updated pose beliefs—an expensive undertaking.

Statistical Dependencies. An aspect of representing the structure of the environment in a map is to model continuity of surfaces. However, most dense mapping techniques are made tractable through the assumption that neighbouring map elements are statistically independent (as we will discuss in Section 2). This allows each element to be updated independently, but at the expense of modelling continuity. As a consequence of this assumption, the resulting models will contain numerous discontinuities. This is problematic for a task like collision prediction, for which it is desirable to have a continuous representation of the environment in order to function accurately. The alternative approach of modelling dependencies between map elements will lead to more accurate map beliefs, but at a higher computational cost.

In order to address the issue of the uncertainty in the robot pose belief, we develop the STM mapping technique using triangular submapping regions, demarcated by landmarks extracted using simultaneous

localisation and mapping (SLAM)—the 2-D hybrid metric map (HYMM) framework [2, 3]. In order to motivate this decision, we briefly explain the HYMM framework, and provide a 3-D extension to it (Section 3). Using this submapping framework, we then develop our STM mapping technique, representing the structure of the environment using a continuous surface (Sections 4 to 5). Finally, we present some experimental results, building STM maps using both simulated and practical data (Section 6).

2. Existing Approaches to Dense Mapping

To motivate our proposal for a new mapping technique, we review and evaluate the existing approaches to dense mapping, and specifically consider the desired attributes a dense map should have.

2.1. Polygonal Mesh Maps

Polygonal meshes are a well-known method of spatial modelling used in computer graphics. A mesh is constructed from a point cloud by linking points together with edges, forming polygons. In an early application, Thrun et al. [4] incrementally built sections of a triangular mesh of indoor environments, subsequently simplifying areas of the mesh by fitting rectangular planes using an online implementation of expectation maximisation. More recently, Wiemann et al. [5] used a k -nearest-neighbours approach to estimate the normals of a triangular mesh, creating a consistent representation of planar surfaces. The resulting mesh was simplified by fusing local polygons with similar normal vectors; however, this process was calculated in post-processing. Zienkiewicz et al. [6] modelled small-scale environments with a fixed topology triangular mesh, and formulated the update procedure probabilistically. By performing weighted optimisation, they were able to iteratively and incrementally obtain solutions to the mesh. Although their approach is formatted probabilistically, it does not capture the uncertainty in the model. Polygonal meshes are not designed to explicitly represent any uncertainty, and therefore cannot incorporate the robot pose belief or sensor uncertainty in a principled manner. They are, however, a popular method for visualising other probabilistic techniques.

2.2. Occupancy Grid Maps

Occupancy grid mapping is one of the most widely used mapping techniques and is considered the de facto representation for dense mapping. Originally developed in 2-D by Moravec and Elfes [7], this technique discretises the map into a volumetric grid, where each volumetric element (voxel) stores the probability that the associated region is occupied. As with all volumetric representations in 3-D, spanning the mapping space with a grid becomes prohibitively expensive, despite the majority of the mapped space being either unoccupied or unobserved. To address this, Hornung et al. [8] developed the OctoMap framework—this is arguably the most used dense mapping framework. Instead of a fixed voxel size, they used octrees to recursively adjust the voxel resolution. Unimportant information, namely the unoccupied or unobserved space, is compressed into coarse voxels, while a finer resolution is maintained for occupied regions. Improving on this, Einhorn et al. [9] developed an adaptive online method of determining the division depth in local regions of the map using the more general kd-tree. Khan et al. [10] used rectangular voxels to compress unoccupied cubic voxels. In recent work, Droschel et al. [11] used an allocentric (robot-centric) grid, where the resolution increases with the distance from the robot. Their approach was also implemented practically, and tested at the DARPA Robotics Challenge. In order to handle the uncertainty of the robot pose belief, Joubert et al. [12] incorporated a beam sensor model into occupancy map updates using Monte-Carlo integration, although this approach was only demonstrated in 2-D. In an attempt to incorporate statistical dependency between 2-D voxels, Thrun [13] used a forward measurement model, and in an offline post-processing procedure optimised for the maximum likelihood map.

Despite their popularity, occupancy grid maps fail to incorporate the dependencies between map elements in an online manner.

2.3. Elevation Maps

The most general way of representing an environment is to use a 3-D dense map; however, some environments are adequately represented as a 2.5-D map—that is, a single axis¹ is constrained to only one value per map element. These elevation maps reduce the dimensionality of the map by associating a single height to each element of a 2-D grid. Early work by Hebert et al. [14] used an elevation map to perform localisation as well as identify footholds for a legged robot. A drawback of elevation maps is their inability to represent overhangs, such as bridges. Triebel et al. [15] dealt with this problem in their method of multi-level surface (MLS) mapping by the clustering measurements in each map element, where the clusters across neighbouring map elements are segmented into elevation classes. Recent work by Fankhauser et al. [16] incorporated the robot pose belief uncertainty into an allocentric elevation map. They achieved this by maintaining a distribution over the spatial uncertainty of a each cell, which is updated over time based on the uncertainty in transformations between the allocentric reference frames. The resulting map is constructed from the weighted average of neighbouring cells, based on each cell’s spatial uncertainty. Their approach was demonstrated for a legged robot. In gamma-SLAM, Marks et al. [17] represent the environment with a 2.5-D precision map, where measurements in each map element are modelled as samples from a Gaussian distribution over the elevation, with an unknown mean and precision. By only considering the precision—marginalising out the mean—their method generated accurate maps for localisation, while also providing a pseudo-metric for traversability. However, their model fails to account for the case where the sensor uncertainty varies at different ranges, and the model disregards height.

Elevation maps are an efficient and effective method of representing environments where a full 3-D representation is unnecessary. However, elevation maps fail to incorporate the statistical dependencies between map elements.

2.4. Signed Distance Function Maps

Over the last decade, advances in depth-camera technology have created affordable and relatively accurate depth sensors. This has given rise to a non-parametric surface representation of the environment using the signed distance function (SDF), commonly used in computer graphics. The SDF calculates the Euclidean distance to the nearest surface, defining positive values to indicate free space, and negative values to indicate occluded regions. Consequently, the surface is implicitly described at the zero-crossings. In KinectFusion, a technique pioneered by Newcombe et al. [18], measurements are fused into a regular 3-D grid of voxels, storing truncated SDF values. Due to memory constraints, this method is only suitable to medium-scale environments. Whelan et al. [19] expanded this to handle large-scale environments by using a sliding window to maintain a local section of the environment as an SDF map, while incrementally converting the regions exiting this window to a triangular mesh. A major advantage in this method is its the ability to adjust the map upon a loop closure. This is achieved through an optimisation procedure over the sensor poses and vertices of the meshed map—creating a globally consistent map. A method by Dai et al. [20], BundleFusion, performs bundle adjustment to optimise over the sensor poses to create accurate SDF maps. Similarly to KinectFusion, this method suffers from memory constraints due to maintaining the complete map in a grid, and is therefore limited to small-scale environments. The standard SDF representation is not probabilistic, and consequently neither sensor uncertainty or pose uncertainty can be incorporated in updating the map. To address this, Dietrich et al. [21] modelled each distance as Gaussian distributed. However, this choice in distribution can yield negative estimates for a positive-only quantity (distance).

Although SDF methods have been shown to generate highly detailed maps in real-time, they have not been widely used in the robotics community due to several drawbacks. Firstly, the SDF can only implicitly describe the surfaces in the environment; when an explicit surface map is required, the SDF map needs to be converted to a mesh. Secondly, as the standard SDF representation is not probabilistic, it cannot model the statistical dependencies between mapping elements. Finally, SDF methods are limited to a single sensor type, namely depth-cameras.

¹Typically the vertical axis.

2.5. Normal Distribution Transform Maps

The normal distributions transform (NDT) mapping model was originally developed by Biber and Strasser [22] as a method for 2-D scan matching, and then independently expanded to 3-D by Takeuchi and Tsubouchi [23], and Magnusson et al. [24]. The resulting volumetric representation maintains a 3-D Gaussian distribution in each voxel. Consequently, measurements falling within a voxel are assumed to be independently and identically distributed (IID) samples drawn a Gaussian distribution, where the sufficient statistics, namely the mean and covariance, can be incrementally calculated. Stoyanov et al. [25] showed that the resulting maps are accurate spatial representations when compared with the methods of occupancy grid mapping and polygonal meshes. They analysed all the methods on simulated and real-world data, comparing receiver operating characteristic (ROC) curves, accuracy, and run-time. NDT mapping was augmented by Saarinen et al. [26] to include the dimension of occupancy, thus creating the NDT occupancy map (NDT-OM). Their representation allowed multi-resolution support for the NDT, while also introducing a temporal measure to handle dynamic environments.

Due to the IID assumption, a drawback to the NDT is that it cannot account for the heterogeneous uncertainty, which is present in the sensor models and the robot pose belief. The map elements are also assumed to be statistically independent.

2.6. Gaussian Process Maps

A popular method of incorporating map element dependencies uses Gaussian process (GP) regression [27]—a method of regression using a non-parametric stochastic model. A set of input training points (measurements of the environment) are used to predict the output at some desired query points. In order to perform this regression, the correlation between points is described by a kernel (covariance), which is parameterised by a set of hyperparameters. GPs can only perform regression on a 1-D output; due to this GPs were initially applied to 2.5-D elevation maps. Lang et al. [28] used an iterative locally adaptive non-stationary kernel, which was able to handle sharp discontinuities without severe smoothing. Extending this, Plagemann et al. [29] used a separate GP to estimate the hyperparameters of each kernel. An ensemble of overlapping GPs was also tiled to cover the mapping region. This method was practically applied to foothold detection of a quadruped robot. Vasudevan [30] implemented a dependent GP to perform offline large-scale terrain modelling on scans of an open mine. Hadsell et al. [31] used a non-stationary kernel where the hyperparameters were a function of the measurement range uncertainty.

In order to use GP regression in full 3-D space, the environment needs to be described implicitly; one method of doing this uses occupancy. Occupancy maps in the context of GP mapping was first proposed by O’Callaghan and Ramos [32], who developed a framework for constructing 2-D GP occupancy maps (GPOMs). To determine the probability of occupancy, an additional probabilistic least-squares classifier was used. Their method was able to incorporate uncertainty in sensor measurements and the robot pose into the map using the unscented transform and Gauss-Hermite quadrature. Jadidi et al. [33] improved on GPOMs by considering the case where the pose uncertainty is significant, and incorporated this uncertainty into a warped GPOM representation using Gauss-Hermite quadrature and Monte Carlo integration. Both these methods, however, were offline post-processing procedures.

The standard GP formulation cannot be applied to online mapping due to two main issues. Firstly, it is required that all the training data be available at once. Secondly, performing online GP regression is intractable due the cubic computational complexity in the amount of training data. An approximate method of addressing both of these issues partitions the training data using a Bayesian committee machine (BCM) [34], which is a method of combining estimators trained on different data by assuming conditional independence. BCMs have a linear computational complexity in the partition size and have been shown to decrease computational time—matching that of even the OctoMap framework [35, 36]. This method, however, combines multiple independently trained estimators, which is an inaccurate representation of the map belief.

Although GPs do not assume statistical independence between map elements, this comes at a prohibitive computational cost, and due to this GPs has been primarily limited to offline mapping. Their performance is also largely dependent on suitable hyperparameters, which can require optimisation throughout the mapping

Table 1: Comparison of mapping techniques across different attributes. We also show our stochastic triangular mesh (STM) mapping technique for comparison.

Mapping Technique	Incorporate Uncertainty	Incremental Updates	Update Efficiency	Statistical Dependencies	Explicit Surface
Polygonal Mesh	✗	✗	$\mathcal{O}(N)$	✗	✓
Occupancy Grid	✓	✓	$\mathcal{O}(N)$	✗	✗
Elevation	✓	✓	$\mathcal{O}(N)$	✗	✓
SDF	✗	✓	$\mathcal{O}(N)$	✗	✗
NDT	Not in measurements	✓	$\mathcal{O}(N)$	✗	✓
GP	✓	✗	$\mathcal{O}(N^3)$	✓	✓
Hilbert	Not in the map	✓	$\mathcal{O}(N)$	✓	✗
STM	✓	✓	$\mathcal{O}(N)$	✓	✓

process. The resulting map is also a jointly Gaussian distribution over all the query points, which can become prohibitively expensive to maintain.

2.7. Hilbert Maps

A more recent method of incorporating the dependencies between map elements was introduced by Ramos and Ott [37]. Their approach, Hilbert maps, aims to generate a continuous occupancy representation of the environment. To achieve this, spatial measurements are projected to a high-dimensional feature space, wherein a simple linear classifier, namely logistic regression, is incrementally trained using stochastic gradient descent. The resulting representation is a parametric occupancy map of the environment. The robot pose belief and sensor uncertainties are also incorporated into the features using numerical integration. To improve efficiency, Doherty et al. [38] used an approach of fusing local maps, whereby multiple logistic regression classifiers could be incrementally combined. Guizilini and Ramos [1] proposed an efficient Hilbert maps approach by clustering measurements to decrease the dimensionality of the feature vectors. This efficient extension to the Hilbert maps framework was able to achieve training speeds rivalling that of the OctoMap framework. However, as a grid is not specified during training, this results in significantly poorer performance when querying the map in comparison to OctoMap.

Hilbert maps do not represent the uncertainty in the resulting map and therefore cannot be truly considered a probabilistic representation of the environment. The Hilbert maps framework has also only been demonstrated using accurate LiDAR sensors, and whether the approximations made will expand for less accurate sensors—like stereo cameras—is unclear.

2.8. Evaluation

The main attributes of the existing mapping techniques are summarised in Table 1. We also include our proposed mapping technique—stochastic triangular mesh (STM) mapping. From this we highlight a few important points related to the existing techniques:

Robot pose belief uncertainty. The majority of probabilistic mapping techniques—bar NDT mapping—have the ability account for the uncertainty in the robot pose belief by marginalising it out using numerical integration²; this increases the uncertainty in the measurements, consequently increasing the map uncertainty.

²Another method of considering the robot pose belief—applicable to all mapping techniques—would be using a Rao-Blackwellised particle filter [e.g. 39]. Here a set of random samples (particles) over the robot pose belief each maintain a map. However, this approach does not scale well in 3-D as it requires maintaining multiple maps, which is already expensive for a single dense map.

Although this more accurately represents the belief over the environment, if the uncertainty in the robot pose belief is significant, this could render the map essentially useless. Additionally, marginalising out the robot pose belief removes the dependencies between poses. This is again a problem when there are significant changes to the beliefs over previous poses, as the affected areas of the map need to be recalculated. A popular approach of alleviating these issues is to perform submapping, which we will subsequently discuss in depth (Section 3).

Statistical dependencies. Most existing mapping techniques cannot incorporate statistical dependencies between map elements. Of the two main techniques that can, GP mapping comes at a intractable computational cost, and Hilbert maps do not capture any uncertainty in the resulting map, which does not accurately model the belief over the environment. In STM mapping, we enforce continuity in the model, which causes statistical dependencies between map elements; however, this only comes at a linear computational cost and still maintains a probabilistic map (Section 4).

Explicit surface models. The existing dense mapping techniques either model the underlying surfaces in the environment explicitly or implicitly. An explicit surface representation is arguably more useful, because some methods of collision prediction [40, 41] require an explicit surface representation. An explicit surface can be extracted from an implicit surface representation; however, this requires an extra step of computation, and results in a model which does not represent any surface uncertainty. For example, an occupancy grid map could be converted to an explicit surface by thresholding the probability of occupancy. We therefore opt for an explicit surface representation of the environment (Section 4).

Incremental Updates. Being able to incrementally update the map is critical for online operation. However, to produce an accurate map belief, it is just as important to use Bayesian reasoning when incrementally updating the map. Specifically, the map’s current state—based on prior measurements—should be considered as context when fusing new measurements into the map; that is, we should use Bayes’ theorem. The probabilistic techniques that use incremental Bayesian updates—occupancy grid, elevation, and NDT maps—do not incorporate statistical dependencies. Despite being a Bayesian technique, GP maps require the BCM approximation to perform incremental updates, which neglects the map’s current state when updating. Additionally, the Hilbert maps method cannot represent the uncertainty in its estimates of the map, as it follows a frequentist approach. In STM mapping, we incorporate incremental Bayesian updates into a continuous representation of the environment (Section 4).

Given this evaluation of existing dense mapping techniques and comparison with our proposed technique, we believe that STM mapping constitutes a valuable contribution to the field of mapping for mobile robots. In the remainder of this paper, we develop and test the STM mapping technique.

3. Inertial Reference Frames in Dense Mapping

The uncertainty in the robot pose belief is ever-present when performing online dense mapping. If the robot pose belief contains significant uncertainty, it creates problems when incorporating measurements into the dense map. In this section, we explore submapping—an approach that reduces the effect of the uncertainty in the robot pose belief—and motivate our choice of submapping framework in the STM mapping technique.

All robotic systems are described in terms of inertial reference frames (IRFs). When discussing the issue of robot pose belief uncertainty in dense mapping, it is important to understand the effect that the choice of IRF has on the resulting map. Some mapping techniques have used an allocentric IRF to ensure that the region of the map currently surrounding the robot has lower uncertainty [16] or a finer grid resolution [11]. In contrast, most mapping techniques focus on building globally consistent maps in a fixed, single-privileged IRF—often referred to as a global IRF. Due to the compounding effect of uncertain motion on the robot pose belief, regions of the map further away from the origin of the chosen IRF are increasingly uncertain; in the absence of absolute position sensing, this uncertainty is unbounded. Furthermore, when performing SLAM in a global IRF and loop closure is performed, large changes in beliefs over previous robot poses

can be induced. Despite this, the *relative* uncertainty between successive robot poses is bounded by the—typically confident—motion dynamics. The submapping approach takes advantage of this by segmenting the environment into several submaps, each with its own IRF. This approach is used in some of the recent state-of-the-art vision-based SLAM techniques, namely LSD-SLAM by Engel et al. [42], and ORB-SLAM by Mur-Artal and Tardós [43]; both of these techniques use keyframes as intermediate submaps during SLAM. In the case of dense mapping in indoor environments, the map can be semantically segmented by room [44]. In general environments, a typical method of defining submaps uses overlapping rectangular cuboids to span the mapping space [45, 46]. However, this causes two issues: the map contains redundant regions, and it is non-trivial to accurately describe new measurements in terms of the IRFs of previously-observed submaps. Hybrid metric maps (HYMMs) [2, 3] is a 2-D submapping technique that addresses both of these issues by using relative IRFs based on the sparse landmark map obtained from SLAM. In Section 3.1 we review the HYMM framework and present a 3-D extension to it. Utilising this framework, we then present a principled method of decoupling measurements of the environment from the robot pose belief (Section 3.2).

Notational remark. A point in the global IRF, \mathbf{x} , is expressed in the body reference frame (RF) of the robot as \mathbf{x}^B , and in a relative IRF as \mathbf{x}^R .

3.1. Relative Inertial Reference Frames

The HYMM submapping technique segments the environment by constructing a triangular mesh between selected landmarks (Figure 1a). A relative IRF is associated with each triangular submap, defined in terms of the three landmarks at the vertices of the triangular region. To elucidate this definition, consider a submap demarcated by the convex hull of the landmarks \mathbf{l}_0 , \mathbf{l}_α and \mathbf{l}_β . A 2-D point, \mathbf{m} , in the global IRF can be described by

$$\begin{aligned}\mathbf{m} &= \alpha(\mathbf{l}_\alpha - \mathbf{l}_0) + \beta(\mathbf{l}_\beta - \mathbf{l}_0) + \mathbf{l}_0 \\ &= \alpha\mathbf{a} + \beta\mathbf{b} + \mathbf{l}_0.\end{aligned}\tag{1}$$

For \mathbf{m} to be within the submap, α and β must satisfy

$$\alpha + \beta \leq 1 \quad \text{and} \quad \alpha, \beta \in [0, 1].\tag{2}$$

The 2-D relative IRF axes are defined by \mathbf{a} and $\mathbf{b} - \mathbf{l}_0$ is an offset—and (α, β) are the coordinates of a 2-D point \mathbf{m} in the relative IRF.

To extend the 2-D relative IRFs of the HYMMs to 3-D, a third axis is required. One could project the 3-D landmarks onto the horizontal plane and use the vertical axis of the global IRF. However, this approach couples the relative IRF to the global IRF, negating the true benefits of a relative IRF. Guivant et al. [2] suggested—but did not develop—two ideas of extending HYMMs to 3-D. The relative IRF axes could be constructed using four landmarks, forming tetrahedral submapping regions; however, it could be impractical to adequately span the mapping space. Alternatively, the 2-D approach can be adapted to 3-D by defining the submapping region being normal to the triangular faces of the 3-D landmark mesh. We develop the latter approach, extending the relative IRF to 3-D by introducing the third axis as

$$\mathbf{n} = \frac{\mathbf{a} \times \mathbf{b}}{\|\mathbf{a} \times \mathbf{b}\|}.\tag{3}$$

Using this definition, a 3-D point, \mathbf{m} , can be described as

$$\begin{aligned}\mathbf{m} &= \alpha\mathbf{a} + \beta\mathbf{b} + \gamma\mathbf{n} + \mathbf{l}_0 \\ &= [\mathbf{a} \quad \mathbf{b} \quad \mathbf{n}] \mathbf{m}^R + \mathbf{l}_0,\end{aligned}\tag{4}$$

where $\mathbf{m}^R = [\alpha \quad \beta \quad \gamma]^\top$ is a point in the 3-D relative IRF (Figure 1b). The constraints in Equation (2) also hold for \mathbf{m} to fall within the submap.

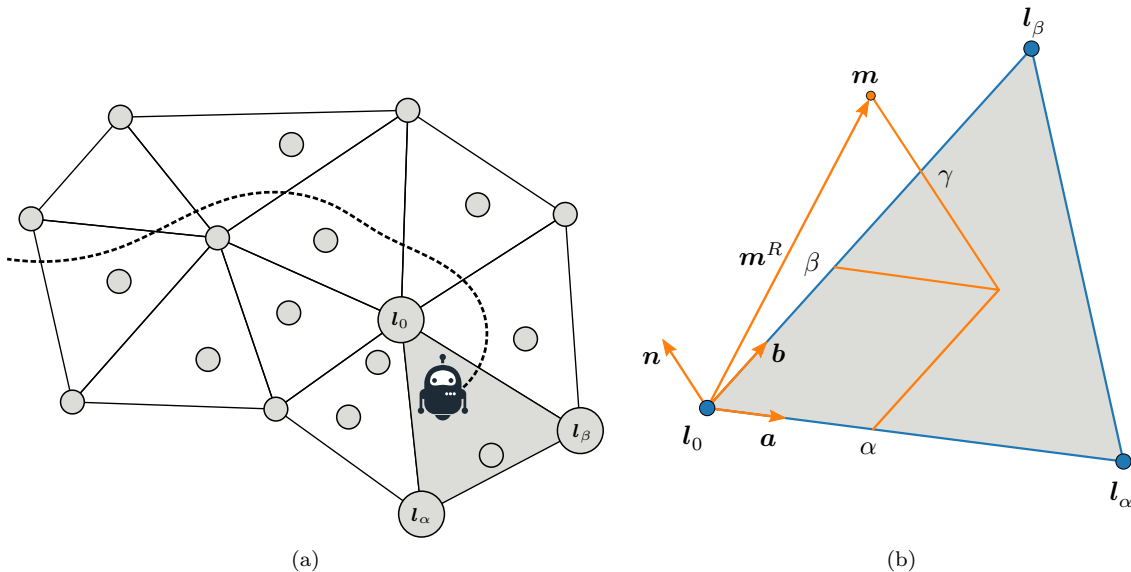


Figure 1: (a) The hybrid metric map (HYMM) submapping method [2, 3] segments the environment using landmarks[†]. (b) In our 3-D extension to the HYMM representation, a point \mathbf{m} within a submap can be fully described relative to these landmarks.

[†]The robot icon was adapted from an original by SimpleIcon from Flaticon.

There is, however, a caveat to using this relative IRF description. As the definition of the relative IRF relies on landmarks, it is necessary for the chosen landmarks to be robustly and persistently identifiable. While this is still an open problem for general environments, given the progress that has been made in the past decade into feature and place recognition [47], we believe that this will be possible in the future. Despite this, there are practical applications, in more controlled environments, where easily identifiable landmarks could be manually placed in the environment—for example in land surveying, 3-D object reconstruction, or factory operation. We practically demonstrate an example of such an application in Section 6.4.

3.2. Decoupling Dense Measurements from the Robot Pose Belief

With the relative IRF definition in hand, we now present a method of decoupling measurements of the surface of the environment from their associated robot pose beliefs. Consequently, this method decouples the process of localisation from that of dense mapping. We achieve this decoupling by transforming surface measurements from the RF of the robot to the relative IRF of the associated submap—as opposed to transforming to the global IRF.

We model the process of observing a point on the surface of the environment (in the RF of the robot) using a sensor beam model, whereby a noisy measurement, \mathbf{z}^B , is generated by a point, \mathbf{m}^B , on the environment surface. Most sensors observe multiple environment surface points at a single time-step. We denote the sequence of measurements as $Z^B = (z_i^B)$ and the associated environment surface points as $M^B = (\mathbf{m}_i^B)$. Assuming an uninformative prior over M^B , we can calculate the belief over M^B as

$$\mathcal{B}(M^B) \triangleq p(M^B|Z^B) \propto \prod_i p(z_i^B|\mathbf{m}_i^B), \quad (5)$$

where the belief distribution, denoted by $\mathcal{B}(\cdot)$, is the posterior distribution over some random variables given all evidence. The conditional distribution $p(z_i^B|\mathbf{m}_i^B)$ describes the measurement model, which is

known beforehand for each sensor. Following from this, the belief over M^B and the SLAM states—the current robot pose, \mathbf{x} , and the sparse landmark map, L , in the global IRF—can be factorised as

$$\begin{aligned} \mathcal{B}(\mathbf{x}, L, M^B) &\triangleq p(\mathbf{x}, L, M^B | U, Y, Z^B) \\ &\approx \underbrace{p(\mathbf{x}, L | U, Y)}_{\mathcal{B}(\mathbf{x}, L)} \underbrace{p(M^B | Z^B)}_{\mathcal{B}(M^B)}, \end{aligned} \quad (6)$$

where $U = (\mathbf{u}_t)$ is the sequence of robot control commands, and $Y = (\mathbf{y}_t)$ is the sequence of landmark measurements. This factorisation makes the assumption that M^B is conditionally independent of the SLAM states given Z^B . It should also be noted that $\mathcal{B}(\mathbf{x}, L)$ is the result of performing SLAM. Although some SLAM algorithms only calculate the maximum a posteriori (MAP) estimate of this belief, we only consider SLAM algorithms that calculate the full belief distribution.

Going forward, we assume $\mathcal{B}(\mathbf{x}, L, M^B)$ to be Gaussian distributed. This does not necessarily limit the SLAM algorithm to one that makes the Gaussian assumption, but simply requires an algorithm where the resulting belief distribution can be projected onto the Gaussian family of distributions—for example by using moment matching.

To transform M^B to the relative IRF, it must first be transformed to the same IRF as the SLAM states—the global IRF. We use the unscented transform (UT) [48, 49] to transform the environment surface points from the body RF to the global IRF, $M^B \rightarrow M$, and then from the global to the relative IRF, $M \rightarrow M^R$. The transformation $M^B \rightarrow M$ is determined by the robot pose in the global IRF, \mathbf{x} . As a consequence of this, M and \mathbf{x} are statistically dependent, and therefore in general, the belief distribution over all the states in the global IRF, $\mathcal{B}(\mathbf{x}, L, M)$, cannot be factorised. If dense mapping was performed in the global IRF, then the global IRF measurement belief, $\mathcal{B}(M)$, would be incorporated into the map. In order for this mapping process to be tractable, the environment points are assumed to be statistically independent of one another; however, this is almost never the case, because of the transformation to the global IRF, they are usually highly correlated with one another (as we will show subsequently).

In order to decouple the process of dense mapping from the robot pose, we need to remove the statistical dependency between M and \mathbf{x} . Transforming M to the relative IRF achieves this through an important characteristic of SLAM: as clusters of neighbouring landmarks are often observed from a single robot pose—or from successive robot poses—these landmarks are highly correlated³. Therefore, although the marginal belief over each landmark in the global IRF can contain significant uncertainty, the relative positions between neighbouring landmarks are known with little uncertainty. More importantly, the landmark correlation increases monotonically with the number of measurements [50], and in the limit, becomes perfectly correlated for the linear Gaussian case [51]. In the case of perfect correlation, there is no uncertainty between the relative landmark positions. We illustrate the effect of various degrees of correlation on the relative landmark positions for a synthetic Gaussian belief over three 2-D landmarks (Figure 2). For perfect linear correlation, the triangles formed by each 6-D sample are identical in shape, whereas the shapes are inconsistent if there is no correlation. In practice, only high correlations between landmarks are achievable, although Nieto et al. [3] showed that the relative uncertainty between landmarks is sufficiently low for relative IRFs to be used in mapping.

Similarly, the robot pose will be highly correlated with nearby landmarks, and consequently the relative positions of the robot pose and landmarks will also be accurately known. In the ideal case where the robot and landmarks positions in the global IRF are perfectly correlated, their relative positions would be perfectly known. If we then describe M with respect to the landmarks (that is, transforming $M \rightarrow M^R$), M^R would be statistically independent of both the landmarks and the robot pose. This is because the relative positions of the robot and landmarks would be known perfectly, and therefore the uncertainty in the belief over M^R would only stem from measurement uncertainty. Although the relative positions are never perfectly known,

³The degree of statistical dependency can be quantified using linear correlation—specifically, using the Pearson correlation coefficient, $\rho \in [-1, 1]$. In the Gaussian case, linear correlation equates to statistical dependency; that is, $\rho = 0$ equates to statistical independence, and $\rho = \pm 1$ equates to perfect linear dependence.

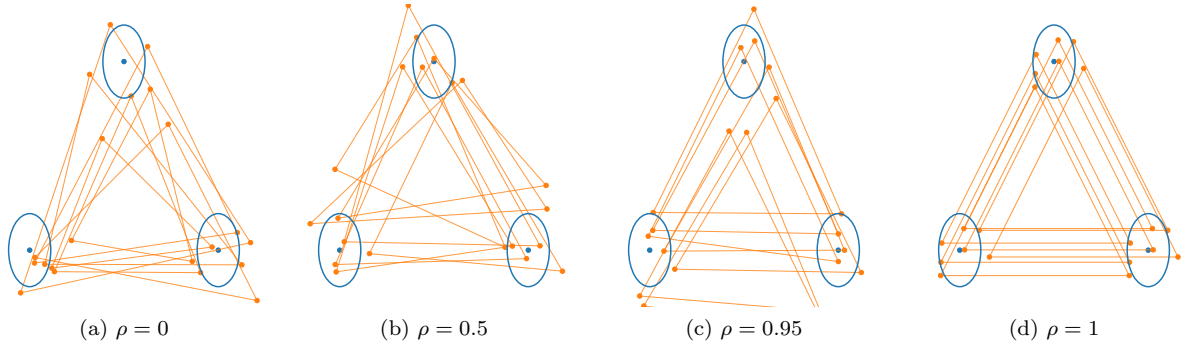


Figure 2: The effect of the degree of linear correlation on the relative positions of three 2-D landmarks. The correlation is quantified using the Pearson correlation coefficient, ρ , for a synthetic Gaussian belief over the landmarks. Shown in blue are the marginal distributions of each landmark—the ellipses indicate the first standard deviations. Each orange triangulation of points represents a single 6-D sample from the joint distribution over all three landmarks.

they are usually accurately known and it is reasonable to approximate the belief over the SLAM states and M^R as statistically independent

$$\mathcal{B}(\mathbf{x}, L, M^R) \approx \mathcal{B}(\mathbf{x}, L)\mathcal{B}(M^R), \quad (7)$$

where

$$\mathcal{B}(M^R) \propto \prod_i p(z_i^R | \mathbf{m}_i^R). \quad (8)$$

To illustrate the validity of this approximation, we visualise the absolute value of the Pearson correlation coefficient matrix for the Gaussian belief distributions $\mathcal{B}(\mathbf{x}, L, M)$ and $\mathcal{B}(\mathbf{x}, L, M^R)$ of a practical stereo vision dataset (Figures 3a and 3b). In $\mathcal{B}(\mathbf{x}, L, M)$ we see that there is indeed a high correlation between \mathbf{x} , L and M . Upon transforming $M \rightarrow M^R$, the resulting belief $\mathcal{B}(\mathbf{x}, L, M^R)$ has negligible correlations between the SLAM states and M^R . The correlations are almost zero, which equates to SLAM states and M^R being approximately statistically independent⁴. Therefore, this process of transforming to a relative IRF decouples the process of dense mapping from the robot pose.

The main advantage of this decoupling process is highlighted in the scenario where loop closure is performed. The belief over the environment surface points in the relative IRF is decoupled from the SLAM states, hence when the belief over the SLAM states changes due to loop closure, the environment surface points no longer need to be reintegrated into the map—as would be required in a global IRF. Instead, the burden is placed on the SLAM algorithm to maintain (or allow the extraction of) marginal distributions over the landmarks demarcating the submaps, which is a far more tractable approach.

In order to evaluate the efficacy of performing dense mapping in a relative IRF—as opposed to a global IRF—we compare the uncertainty in the beliefs over the environment surface points in a relative and global IRF. For the case of mapping in a relative IRF, we consider our approximate belief $\mathcal{B}(M^R)$ (Equation (8)). We also consider the ideal case where our statistical independence approximation is exact—that is, the robot pose and landmarks are perfectly correlated, or in other words, the relative positions between \mathbf{x} and L are perfectly known. The uncertainty in this ideal belief, $\mathcal{B}_{\text{ideal}}(M^R)$, is solely dependent on the measurement uncertainty. For the case of mapping in a global IRF we consider the belief over the environment surface points in a global IRF, $\mathcal{B}(M)$. To compare the beliefs in the relative IRF with that of the global IRF, we need to evaluate all the beliefs using the same units. We therefore deterministically transform $\mathcal{B}(M)$, to the relative IRF using the maximum likelihood value of the landmarks; we denote the resulting belief $\mathcal{B}_{\text{global}}(M^R)$. The resulting comparison of all the beliefs is shown in Figure 3c. From this we can conclude that

⁴Jointly Gaussian distributed variables are statistically independent if and only if they are uncorrelated.

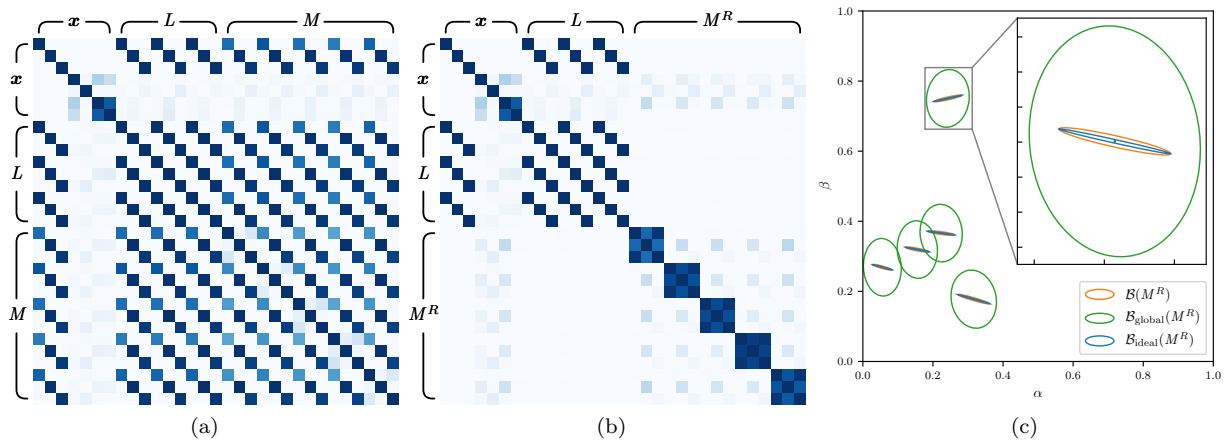


Figure 3: A visualisation of the absolute value of the Pearson correlation coefficient matrix (the darker, the more correlated) for the Gaussian belief distributions[†] $\mathcal{B}(\mathbf{x}, L, M)$ and (b) $\mathcal{B}(\mathbf{x}, L, M^R)$. In (b) the block 3×3 block diagonals are from the individual 3-D environment surface points. (c) A comparison of the uncertainty in the beliefs over the environment surface measurements in a relative and global inertial reference frame (IRF). Our approximate belief, $\mathcal{B}(M^R)$, is compared to $\mathcal{B}_{\text{ideal}}(M^R)$ and $\mathcal{B}_{\text{global}}(M^R)$ (see the text for further details on the belief definitions). The ellipses outline the first standard deviations of the respective belief distributions. The data in this visualisation was taken from a practical stereo vision dataset.

[†]We denote the current robot pose and landmark map in the global IRF, \mathbf{x} and L respectively, and the environment surface points in the global IRF, M , and the relative IRF, M^R .

the uncertainty in belief over the environment surface point used for dense mapping can be significantly less when using a relative IRF instead of a global IRF. Additionally, the uncertainty in the belief becomes almost solely dependent on the measurement uncertainty. Nieto et al. [3] noted similar effects when representing other landmarks in a relative IRF; that is, a dramatic decrease in the correlation between landmarks in the relative and global IRFs, and a decrease in the marginal landmark belief uncertainty in the relative IRF.

In this section we presented a method of decoupling the robot pose from the process of dense mapping. By transforming the information from the measured environment surface points to a relative IRF, we have approximately removed their statistical dependence on the robot pose. Next we look at incorporating this information into our model of the environment.

4. The Stochastic Triangular Mesh Map

Based on the highlighted drawbacks of the existing mapping techniques (Section 2.8), we propose a mapping technique that explicitly models the surface of the environment using a stochastic triangular mesh (STM); that is, a triangular mesh consisting of stochastic surface elements (surfels), forming a continuous representation of the surface of the environment (Figure 4).

Most of the existing explicit surface mapping techniques operate under the approximation that the map *can* exactly model the surface of the environment. A STM map, on the other hand, accounts for the fact that the surface of the environment cannot be exactly modelled with deterministic map elements; instead, the surface of the environment is treated as a *stochastic process*. Additionally, even if it is possible to represent the environment exactly, the representation would be very wasteful; we rather summarise the surface information relevant to the application. In contrast with most mapping techniques, a STM map also captures the structure of the environment by enforcing continuity in the model. Although the principle is

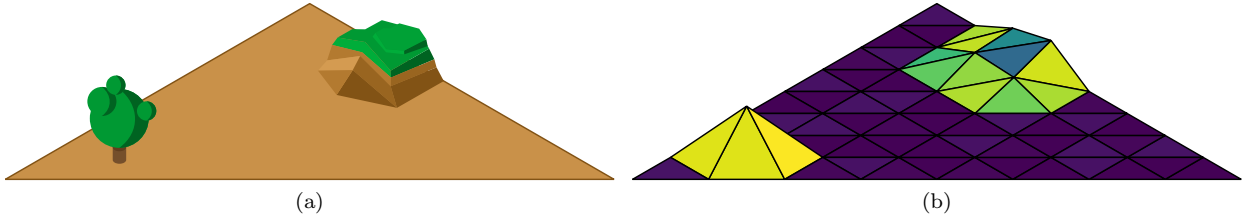


Figure 4: (a) A hypothetical environment within a triangular submap[†], and (b) a depiction of the corresponding a stochastic triangular mesh (STM) map. Each triangular surface element (surfel) in the mesh is coloured according to its planar deviation—the deviation of the actual surface of the environment from the triangular planes (the lighter, the higher the deviation.)

[†]The hill and tree icons were adapted from an original by sceneit from Vecteezy.com.

similar to Gaussian process mapping, we are able to update on the model incrementally and in a scalable fashion.

Following the aforementioned submapping method (Section 3), we develop the STM map within a triangular submap. We partition the submap into a regular triangular grid by recursively subdividing the horizontal (α - β) plane into equisized triangular grid elements (Figure 5). The surface of the environment within each grid element—the region normal to the grid element—is modelled by the STM map using a surfel. The submap division is performed until a desired grid element size is achieved. Depending on the application, this could be simply chosen based on the dimensions and physical capability of the robot. In general, it would be more sensible to perform this partitioning in an adaptive manner, although we do not address this in the current implementation, and will discuss this in future work (Section 7).

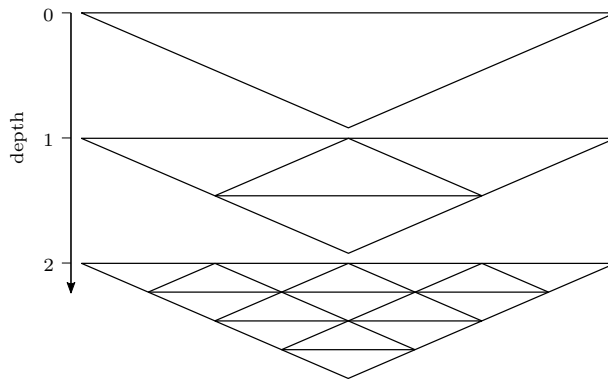


Figure 5: The recursive division of a triangular submap into equisized triangular grid elements.

In the remainder of this section, we discuss how each surfel in a STM map models the surface of the environment. Subsequently, we discuss performing incremental Bayesian inference on a STM map (Section 5). It should also be noted that we develop the STM map within the relative inertial reference frame (IRF) of a submap, and consequently, all variables are assumed to be defined in the relative IRF. However, without loss of generality, this representation could also be applied in a global IRF framework by defining the IRF accordingly, which we demonstrate in Section 6.5.

4.1. Surface Element Model

A stochastic triangular mesh (STM) map consists of triangular surface elements (surfels), which together form a continuous representation of the surface of the environment within the submap. We assume that the

surface of the environment within the submap can be adequately represented using a 2.5-D map—at any coordinate on the horizontal plane, the environment normal to this plane need only be described using a single height. Therefore, associated with each grid element is a triangular surfel that models the surface of the environment within the grid element—the region normal to the grid element.

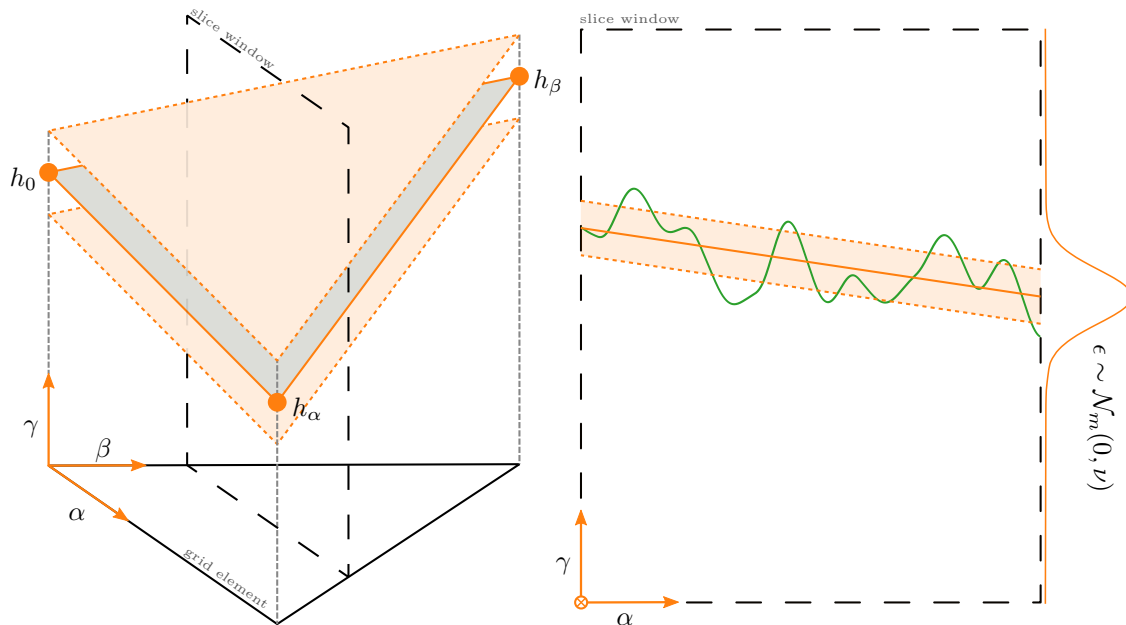


Figure 6: (left) The surface element (surfel) model, consisting of a mean plane—parameterised by the vertex heights $\mathbf{h} = [h_0, h_\alpha, h_\beta]^\top$ —and a planar deviation ν . (right) A 2-D slice of the surfel (orange) of an underlying surface (green). The shaded region indicates the one standard deviation confidence interval. $\mathcal{N}_m(\cdot)$ denotes the moment form of a Gaussian distribution.

If we initially consider a map with a single grid element, the maximum length along both the α - and β -axes within the grid element will be unity—Equation (2). The associated surfel models the surface of the environment within the grid element as a stochastic process—a mean plane and a homoscedastic⁵ deviation from it, normal to the grid element (Figure 6). This simple model does not try to exactly represent the actual surface of the environment, but summarises the key aspects of the surface instead. More precisely, a point on the surface of the environment at some given coordinates (α, β) is modelled by the stochastic process

$$\begin{aligned} \gamma &= f(\alpha, \beta, \mathbf{h}) + \epsilon \\ &= [1 - \alpha - \beta \quad \alpha \quad \beta] \mathbf{h} + \epsilon, \end{aligned} \quad (9)$$

where $f(\alpha, \beta, \mathbf{h})$ describes a point on the mean plane, and $\epsilon \sim \mathcal{N}_m(\epsilon; 0, \nu)$ ⁶ models the deviation of the actual surface from the mean plane. We will refer to the variance of the stochastic process, ν , as the planar deviation. The mean plane is specified using the normal heights at each of the vertices of the grid element

$$\mathbf{h} = \begin{bmatrix} h_0 \\ h_\alpha \\ h_\beta \end{bmatrix}, \quad (10)$$

⁵A stochastic process is *homoscedastic* when the process variance is constant and finite.

⁶For a Gaussian distribution, we denote the canonical form $\mathcal{N}_c(\cdot)$, and the moment form $\mathcal{N}_m(\cdot)$.

where h_0 , h_α , and h_β are the heights at $(\alpha, \beta) = (0, 0)$, $(1, 0)$ and $(0, 1)$ respectively. Consequently, the surfel model is parameterised by \mathbf{h} and ν , which we combine into a single parameter vector $\theta = [\mathbf{h} \ \nu]^\top$. This simple stochastic process allows us to account for a wide range of surfaces by essentially summarising the underlying environment within the grid element. It should be noted that we follow a Bayesian modelling approach, treating the map parameters as random variables. We specifically model the each surfels heights as Gaussian distributed, and the planar deviation as inverse-gamma distributed. We expand on this when discussing performing inference on the model (Section 5).

In order to generalise this definition of the surfel model from a single to multiple grid elements within a submap, we normalise each grid element—scaling the maximum length of the α - and β -axes to unity, and shifting to the origin. This normalisation does not affect the values of the surfel parameters, θ , which are defined with respect to the γ -axis. Additionally, as this is a deterministic linear operation, the Gaussian measurement distributions in this normalised grid element will remain exactly Gaussian distributed, which will be important when performing inference on the surfel model parameters (Section 5).

To create a continuous representation, the mean planes of surfels in contiguous grid elements are constrained to be continuous; that is, the heights at their shared vertices should be equal (Figure 7). However, we do not enforce any constraints on the planar deviations between surfels. The continuous surface in a submap formed by the mean plane in each surfel describes the mean mesh, which is parameterised by the ordered set of unique vertex heights, H . The stochastic deviation from this mean mesh is parameterised by the ordered set of planar deviations in each surfel, V . Both H and V fully parameterise a STM map, which we can combine into a single ordered set θ .

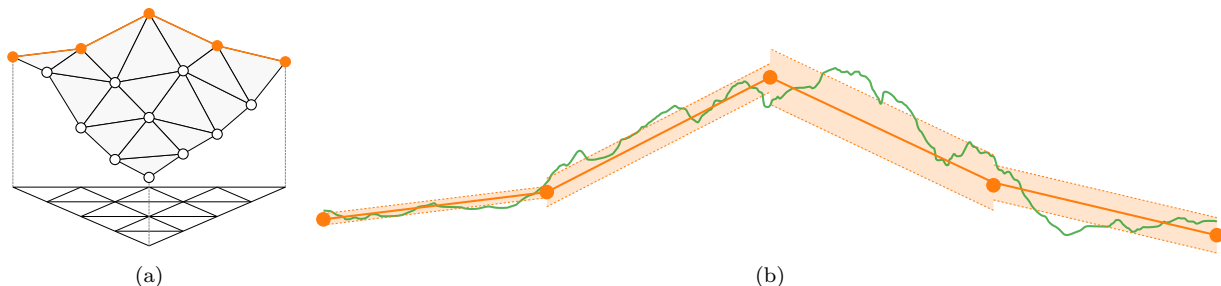


Figure 7: A stochastic triangular mesh (STM) forms a continuous representation of the surface of the environment. We visualise (a) the mean mesh, and (b) a slice through the STM map (orange) of an underlying surface (green). The shaded region indicates the one standard deviation confidence interval in the respective surfels.

We have defined how the constituent surfels of a STM map model the environment; we now seek to determine the parameter values for a STM map based on measurements of the surface of the environment—in other words, to perform inference.

5. Model Inference

Based on the definition of a STM map, we now wish to infer the values of the map parameters, θ , for some given noisy measurements of the surface of the environment, $Z = \mathbf{Z}$. We follow a Bayesian modelling approach, maintaining a belief distribution⁷ over the map parameters. We would therefore ideally like to calculate the joint belief distribution over all the map parameters

$$\mathcal{B}(\theta) = p(\theta | Z = \mathbf{Z}). \quad (11)$$

⁷A belief distribution is the posterior distribution over some states given all the relevant evidence.

However, for large maps this would quickly become intractable to store, as the storage grows quadratically with the number of surfels in the map (for our choice of continuous parametric distributions). To circumvent this issue, we instead directly calculate the marginal belief for each surfel’s parameters

$$\mathcal{B}(\boldsymbol{\theta}) = p(\boldsymbol{\theta}|Z = \mathbf{Z}), \quad (12)$$

for which storage grows linearly with each added surfel.

Next we will look at calculating each surfel’s belief independently of the rest of the map (Section 5.1); this is equivalent to neglecting the continuity constraints between surfels. Building upon this, we expand to performing inference on the full model (Section 5.2). Finally, we summarise the inference algorithm for a STM map, and discuss the implementation thereof (Section 5.3).

5.1. Single Surfel Inference

We initially consider each surfel in isolation, and wish to calculate the belief distribution over a single surfel’s parameters, $\boldsymbol{\theta} = [\mathbf{h} \ \nu]^\top$, from noisy measurements associated with the respective grid element⁸. We combine this approach to handle multiple surfels in Section 5.2, but it is useful to first consider this perspective before performing inference on the full model.

Most probabilistic problems involve several random variables; probabilistic graphical models (PGMs)⁹ provide a compact graphical representation over this complex high-dimensional space, which is useful in both modelling and performing inference. There are many different PGMs for different types of problems (or questions); in our case we focus on three types of PGMs: Bayesian networks, factor graphs, and cluster graphs. A *Bayesian network*, or *belief network*, represents the conditional independence assumptions in the joint distribution as a directed graph between random variable nodes. The surfel model we use is shown as a Bayesian network in Figure 8a, which equivalently represents the factorisation over the joint distribution

$$\begin{aligned} p(\boldsymbol{\theta}, M, Z) &= p(\boldsymbol{\theta}) \underbrace{\prod_i p(\mathbf{z}_i | \mathbf{m}_i)}_{p(M, Z | \boldsymbol{\theta})} \overbrace{p(\gamma_i | \alpha_i, \beta_i, \boldsymbol{\theta}) p(\alpha_i) p(\beta_i)}^{p(\mathbf{m}_i | \boldsymbol{\theta})}, \end{aligned} \quad (13)$$

where $Z = (\mathbf{z}_i)$ is the sequence of noisy measurements corresponding to the points on the surface of the environment, $M = (\mathbf{m}_i)$, as mentioned in Section 3.2. This factorisation of the joint distribution models the generative process of measurements—the model parameters describe where actual points on the surface in the environment lie, and these points are observed through measurements of the environment. In the measurement mode, $p(\mathbf{z}_i | \mathbf{m}_i)$, we assume that a measurement, \mathbf{z}_i , is only dependent on the corresponding point on the actual surface of the environment, \mathbf{m}_i ; this measurement distribution was derived in Section 3.2. In $p(\gamma_i | \alpha_i, \beta_i, \boldsymbol{\theta})$, we assume the height of the surface point, γ_i , is only dependent on the grid element coordinates (α_i, β_i) and the surfel parameters, $\boldsymbol{\theta}$. This is based on the definition of the stochastic process in the surfel model—Equation (9).

From this Bayesian network we can construct a *factor graph* (Figure 8b). It represents the fully factorised functional form of the joint distribution in an undirected graph, where the random variables are linked by the factors they share. These factors can be grouped into clusters, resulting in a *cluster graph* representation (Figure 8c). The combined factors in a cluster are known as the cluster potential, and shared links between clusters are defined by their sepset—a subset of the shared variables. Although there is a unique factor graph for a Bayesian network, the grouping of factors in a cluster graph is, in general, non-unique. We choose to group all the factors inside the plate into a cluster, and the factor outside the plate into a cluster. Both factor and cluster graphs can be used for inference, although we will focus on inference in cluster graphs.

⁸We associate a measurement to a grid element based solely on whether the measurement’s mean lies within the grid element.

⁹For a comprehensive guide to PGMs we refer the reader to Koller and Friedman [52].

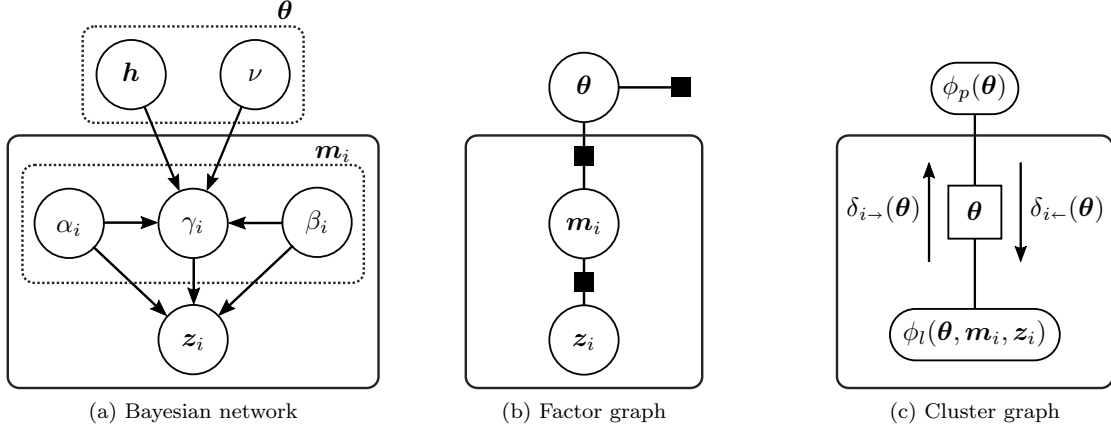


Figure 8: Different types of probabilistic graphical models representing the inference problem for our surfel model. The surfel model parameters, $\boldsymbol{\theta} = [\mathbf{h} \ \nu]^\top$, measurements, \mathbf{z}_i , and corresponding points on the surface of the environment, $\mathbf{m}_i = [\alpha_i \ \beta_i \ \gamma_i]^\top$, are all random variables. We use plate notation, where the solid rectangular plates indicate a repetition of the subgraph therein. (a) The dotted rectangle denotes an expanded vector. (b) Factors are indicated with \blacksquare . (c) Cluster potentials and messages are denoted $\phi(\cdot)$ and $\delta(\cdot)$ respectively, and the sepset between clusters is indicated with \square .

As a cluster graph is the result of grouping factors from the joint distribution, we can equivalently represent the joint distribution as the product over all the cluster potentials

$$p(\boldsymbol{\theta}, M, Z) = \phi_p(\boldsymbol{\theta}) \prod_i \phi_l(\boldsymbol{\theta}, \mathbf{m}_i, \mathbf{z}_i), \quad (14)$$

where we refer to $\phi_p(\boldsymbol{\theta})$ as the *prior cluster potential* and each $\phi_l(\boldsymbol{\theta}, \mathbf{m}_i, \mathbf{z}_i)$ as a *likelihood cluster potential*. We wish to infer the surfel belief for some given measurements, $Z = \mathbf{Z}$. Using Bayes' theorem, we can express this belief in terms of the joint distribution

$$\begin{aligned} \mathcal{B}(\boldsymbol{\theta}) &= p(\boldsymbol{\theta} | Z = \mathbf{Z}) \\ &\propto \int_M p(\boldsymbol{\theta}, M, Z = \mathbf{Z}) dM \\ &\propto \phi_p(\boldsymbol{\theta}) \prod_i \int_{\mathbf{m}_i} \phi_l(\boldsymbol{\theta}, \mathbf{m}_i, \mathbf{z}_i = \mathbf{z}_i) d\mathbf{m}_i. \end{aligned} \quad (15)$$

An equivalent method of calculating this belief is by using message passing. For inference in cluster graphs, the outgoing and incoming messages for each cluster need to be calculated. According to the integral-product algorithm, the outgoing message from the i -th likelihood cluster is defined as

$$\delta_{i \rightarrow}(\boldsymbol{\theta}) = \int_{\mathbf{m}_i} \phi_l(\boldsymbol{\theta}, \mathbf{m}_i, \mathbf{z}_i = \mathbf{z}_i) d\mathbf{m}_i. \quad (16)$$

Similarly, the incoming message to the i -th likelihood cluster is defined as

$$\delta_{i \leftarrow}(\boldsymbol{\theta}) = \phi_p(\boldsymbol{\theta}) \prod_{j \neq i} \delta_{j \rightarrow}(\boldsymbol{\theta}). \quad (17)$$

By comparing Equation (15) with Equations (16) and (17) we can see that the product of these messages equivalently specifies the surfel belief

$$\mathcal{B}(\boldsymbol{\theta}) \propto \delta_{i \rightarrow}(\boldsymbol{\theta}) \delta_{i \leftarrow}(\boldsymbol{\theta}). \quad (18)$$

There is, however, no convenient closed-form solution to either of the messages—and consequently the surfel belief. This is due to nonlinear relationships between the random variables in the likelihood cluster potentials. In order to find a tractable solution to the surfel belief, we have to perform approximate inference. We specifically focus on variational inference¹⁰, which projects a desired (intractable) probability distribution onto an approximating family of distributions. This projection is performed by minimising a chosen information divergence—a measure of similarity—between the exact and approximate distributions. A commonly-used information divergence is the Kullback-Leibler (KL) divergence

$$D_{\text{KL}}(q(x) \parallel p(x)) \triangleq \int_x q(x) \log \frac{q(x)}{p(x)} dx, \quad (19)$$

which is a positive measure of relative entropy between two probability distributions $p(x)$ and $q(x)$ ¹¹. We minimise the exclusive KL divergence to calculate an approximate surfel belief

$$\tilde{\mathcal{B}}(\boldsymbol{\theta}) = \arg \min_{\tilde{\mathcal{B}}(\boldsymbol{\theta}) \in \mathcal{F}} D_{\text{KL}}(\tilde{\mathcal{B}}(\boldsymbol{\theta}) \parallel \mathcal{B}(\boldsymbol{\theta})), \quad (20)$$

where \mathcal{F} is a family of approximating distributions. This process of minimising the exclusive KL divergence is commonly referred to as the *information projection*; alternatively minimising the inclusive KL divergence is referred to as the *moment projection*. As opposed to minimising this global divergence, a group of techniques known as *approximate message passing*¹² distributes the problem of variational inference by instead incrementally performing local projections with the aim of approximately minimising the global divergence. In essence, message passing minimises the global divergence using coordinate descent. This can be explained intuitively in the context of performing inference in a cluster graph. Message passing iteratively approximates each cluster potential; at each iteration, a certain cluster potential is approximated, while keeping all other cluster potentials constant. The constant cluster potentials determine the incoming message of the cluster potential being approximated, and are used as context to update the approximation (how the approximation is updated depends on the chosen divergence measure). This process is repeated until convergence, upon which the global divergence is assumed to be at a (local) minimum.

Performing message passing for our chosen divergence measure is known as variational message passing (VMP) [55]. If we were to instead minimise the inclusive KL divergence (moment projection), this would result in the expectation propagation (EP) message passing technique [56]. A notable property of VMP is that a fixed point in performing message passing is also a stationary point in the global divergence—in other words, minimising local divergences is equivalent to minimising the global divergence. VMP is also the only message passing technique with this property, whereas other message passing techniques only approximate it [54]; this is as a result of VMP using the exclusive KL divergence.

In order to calculate the approximate surfel belief

$$\tilde{\mathcal{B}}(\boldsymbol{\theta}) \propto \tilde{\delta}_{i \rightarrow}(\boldsymbol{\theta}) \tilde{\delta}_{i \leftarrow}(\boldsymbol{\theta}), \quad (21)$$

the approximate messages, $\tilde{\delta}_{i \rightarrow}(\boldsymbol{\theta})$ and $\tilde{\delta}_{i \leftarrow}(\boldsymbol{\theta})$, are calculated by replacing $\phi_l(\boldsymbol{\theta}, \mathbf{m}_i, \mathbf{z}_i = \mathbf{z}_i)$ by an approximating likelihood cluster potential, $\tilde{\phi}_l(\boldsymbol{\theta}, \mathbf{m}_i)$, in Equations (16) and (17). To calculate each approximate likelihood cluster potential, VMP performs a local information projection

$$\tilde{\phi}_l(\boldsymbol{\theta}, \mathbf{m}_i) = \arg \min_{\tilde{\phi}_l \in \mathcal{F}} D_{\text{KL}}(\tilde{\phi}_l \tilde{\delta}_{i \leftarrow} \parallel \phi_l \tilde{\delta}_{i \leftarrow}), \quad (22)$$

where \mathcal{F} is a family of approximating distributions (we omit the arguments of the functions to declutter the notation). It should be noted that this is an iterative process as we must perform this local projection

¹⁰For a review on the principles of variational inference see Blei et al. [53]

¹¹The Kullback-Leibler (KL) divergence is asymmetric— $D_{\text{KL}}(q(x) \parallel p(x)) \neq D_{\text{KL}}(p(x) \parallel q(x))$. If $p(x)$ is exact and $q(x)$ an approximation then $D_{\text{KL}}(q(x) \parallel p(x))$ is referred to as the exclusive KL divergence. The reverse of this, $D_{\text{KL}}(p(x) \parallel q(x))$, is referred to as the inclusive KL divergence.

¹²For a review on message passing techniques see Minka [54].

for each likelihood cluster potential. To make this local projection tractable, we also make the simplifying assumption that each approximating likelihood cluster potential is of the factorised form¹³

$$\tilde{\phi}_l(\boldsymbol{\theta}, \mathbf{m}_i) = \tilde{\phi}_l(\mathbf{h}, \mathbf{m}_i)\tilde{\phi}_l(\nu). \quad (23)$$

This factorisation over disjoint sets of the random variables is a commonly-used approximation referred as the structured mean-field approximation [57]. We choose this structured factorisation in particular as it more accurately represents the exact distribution, compared to a full factorisation. In contrast to other structured factorisation combinations, it groups variables from the same distribution family (as we will soon show). We also assume the prior cluster potential to be of a similar factorised form

$$\phi_p(\boldsymbol{\theta}) = \phi_p(\mathbf{h})\phi_p(\nu), \quad (24)$$

therefore the approximate messages and surfel belief will be similarly factorised.

In order to perform the minimisation in Equation (22), we first need to specify the family of approximating distributions for the factors of $\tilde{\phi}_l(\boldsymbol{\theta}, \mathbf{m}_i)$. For the factor over \mathbf{h} and \mathbf{m}_i , we choose the Gaussian distribution

$$\tilde{\phi}_l(\mathbf{h}, \mathbf{m}_i) = \mathcal{N}_c([\mathbf{h} \ \mathbf{m}_i]^\top; \boldsymbol{\xi}_l, \boldsymbol{\Omega}_l), \quad (25)$$

where $\boldsymbol{\xi}_l$ is the information vector and $\boldsymbol{\Omega}_l$ is the information matrix of the Gaussian distribution in canonical form. For the factor over ν , we choose the inverse-gamma distribution

$$\tilde{\phi}_l(\nu) = \Gamma^{-1}(\nu; a_i, b_i), \quad (26)$$

where a_i is the scale parameter and b_i the shape parameter of the inverse-gamma distribution. The resulting product of these distributions—Equation (23)—should not be confused with a normal-inverse-gamma distribution. In our case this is simply the product of these two distributions without any conditional dependencies.

If we had already calculated the approximate likelihood cluster potential, $\tilde{\phi}_l(\boldsymbol{\theta}, \mathbf{m}_i)$, we could calculate the outgoing message using Equation (16), which would result in the distribution

$$\tilde{\delta}_{i\rightarrow}(\boldsymbol{\theta}) = \underbrace{\mathcal{N}_c(\mathbf{h}; \boldsymbol{\xi}_{i\rightarrow}, \boldsymbol{\Omega}_{i\rightarrow})}_{\tilde{\delta}_{i\rightarrow}(\mathbf{h})} \underbrace{\Gamma^{-1}(\nu; a_{i\rightarrow} - 1, b_{i\rightarrow})}_{\tilde{\delta}_{i\rightarrow}(\nu)}. \quad (27)$$

We assume that the prior cluster potential is also similarly distributed

$$\phi_p(\boldsymbol{\theta}) = \underbrace{\mathcal{N}_c(\mathbf{h}; \boldsymbol{\xi}_p, \boldsymbol{\Omega}_p)}_{\phi_p(\mathbf{h})} \underbrace{\Gamma^{-1}(\nu; a_p, b_p)}_{\phi_p(\nu)}. \quad (28)$$

Both the Gaussian and inverse-gamma families of distributions are of the part of the exponential family [58]. These have the convenient property that the product and division of distributions in the family also results in a distribution in the family [54] (up to a proportionality constant), which amounts to the addition and subtraction of their natural parameters, respectively. We can therefore calculate the approximate incoming message to a cluster, which will be distributed similarly to its constituents

$$\tilde{\delta}_{i\leftarrow}(\boldsymbol{\theta}) = \underbrace{\mathcal{N}_c(\mathbf{h}; \boldsymbol{\xi}_{i\leftarrow}, \boldsymbol{\Omega}_{i\leftarrow})}_{\tilde{\delta}_{i\leftarrow}(\mathbf{h})} \underbrace{\Gamma^{-1}(\nu; a_{i\leftarrow}, b_{i\leftarrow})}_{\tilde{\delta}_{i\leftarrow}(\nu)}. \quad (29)$$

According to Equation (17), the natural parameters of $\tilde{\delta}_{i\leftarrow}(\mathbf{h})$ are calculated as

$$\boldsymbol{\Omega}_{i\leftarrow} = \boldsymbol{\Omega}_p + \sum_{j \neq i} \boldsymbol{\Omega}_{j\rightarrow} \quad \text{and} \quad \boldsymbol{\xi}_{i\leftarrow} = \boldsymbol{\xi}_p + \sum_{j \neq i} \boldsymbol{\xi}_{j\rightarrow}, \quad (30)$$

¹³From this point on, for notational brevity we loosely use the arguments to functions as unique identifiers, namely $f(x) \triangleq f_x(x)$ and $f(y) \not\equiv f(x)$.

and the natural parameters of $\tilde{\delta}_{i\leftarrow}(\nu)$ are calculated as

$$a_{i\leftarrow} = a_p + \sum_{j \neq i} a_{j \rightarrow} \quad \text{and} \quad b_{i\leftarrow} = b_p + \sum_{j \neq i} b_{j \rightarrow}. \quad (31)$$

The same is true for the approximate surfel belief

$$\tilde{\mathcal{B}}(\boldsymbol{\theta}) = \underbrace{\mathcal{N}_c(\mathbf{h}; \boldsymbol{\xi}_h, \boldsymbol{\Omega}_h)}_{\tilde{\mathcal{B}}(\mathbf{h})} \underbrace{\Gamma^{-1}(\nu; a_\nu, b_\nu)}_{\tilde{\mathcal{B}}(\nu)}. \quad (32)$$

According to Equation (21), the natural parameters of $\tilde{\mathcal{B}}(\mathbf{h})$ are calculated as

$$\boldsymbol{\Omega}_h = \boldsymbol{\Omega}_{i \rightarrow} + \boldsymbol{\Omega}_{i \leftarrow} \quad \text{and} \quad \boldsymbol{\xi}_h = \boldsymbol{\xi}_{i \rightarrow} + \boldsymbol{\xi}_{i \leftarrow}, \quad (33)$$

and the natural parameters of $\tilde{\mathcal{B}}(\nu)$ are calculated as

$$a_\nu = a_{i \rightarrow} + a_{i \leftarrow} \quad \text{and} \quad b_\nu = b_{i \rightarrow} + b_{i \leftarrow}. \quad (34)$$

Performing VMP with the structured mean-field approximation therefore allows us to perform tractable inference to obtain an approximation of the surfel belief. Up to this point, we have assumed that we have the approximate likelihood cluster potentials, $\tilde{\phi}_l(\boldsymbol{\theta}, \mathbf{m}_i)$. We will now discuss exactly how to calculate each of the factors of approximate likelihood cluster potentials, and consequently, the outgoing message, $\tilde{\delta}_{i \rightarrow}(\boldsymbol{\theta})$.

5.1.1. Updating Mean Plane Factor

The iterative update of $\tilde{\phi}_l(\boldsymbol{\theta}, \mathbf{m}_i)$ that would perform the local information projection of Equation (22) can be calculated according to the VMP algorithm [55] as

$$\begin{aligned} & \log \tilde{\phi}_l(\boldsymbol{\theta}, \mathbf{m}_i) + \log \tilde{\delta}_{i \leftarrow}(\mathbf{h}) \\ & \propto \left\langle \log \phi_l(\boldsymbol{\theta}, \mathbf{m}_i, \mathbf{z}_i = \mathbf{z}_i) \tilde{\delta}_{i \leftarrow}(\boldsymbol{\theta}) \right\rangle_{\tilde{\mathcal{B}}(\nu)}, \end{aligned} \quad (35)$$

where $\langle \cdot \rangle$ denotes the expectation operation. In order to arrive at a solution to $\tilde{\phi}_l(\boldsymbol{\theta}, \mathbf{m}_i)$, it is convenient to first describe the process of calculating the approximate belief

$$\tilde{\mathcal{B}}(\mathbf{h}, \mathbf{m}_i) \propto \tilde{\phi}_l(\boldsymbol{\theta}, \mathbf{m}_i) \tilde{\delta}_{i \leftarrow}(\mathbf{h}), \quad (36)$$

and then divide out the message $\tilde{\delta}_{i \leftarrow}(\mathbf{h})$ to recover the desired approximate to the cluster potential $\tilde{\phi}_l(\boldsymbol{\theta}, \mathbf{m}_i)$. Rearranging Equation (35) in terms of $\tilde{\mathcal{B}}(\mathbf{h}, \mathbf{m}_i)$ we can calculate the expectation

$$\begin{aligned} \log \tilde{\mathcal{B}}(\mathbf{h}, \mathbf{m}_i) & \propto \left\langle \log \left(\phi_l(\boldsymbol{\theta}, \mathbf{m}_i, \mathbf{z}_i = \mathbf{z}_i) \tilde{\delta}_{i \leftarrow}(\boldsymbol{\theta}) \right) \right\rangle_{\tilde{\mathcal{B}}(\nu)} \\ & = \log p(\gamma_i | \alpha_i, \beta_i, \mathbf{h}, \nu = \nu_B) \\ & \quad + \log p(\mathbf{z}_i = \mathbf{z}_i | \mathbf{m}_i) \\ & \quad + \log \left(p(\alpha_i) p(\beta_i) \tilde{\delta}_{i \leftarrow}(\mathbf{h}) \right), \end{aligned} \quad (37)$$

where

$$\nu_B = \left\langle \nu^{-1} \right\rangle_{\tilde{\mathcal{B}}(\nu)}^{-1} = \frac{b_\nu}{a_\nu}. \quad (38)$$

In order to find an analytical expression for $\tilde{\mathcal{B}}(\mathbf{h}, \mathbf{m}_i)$, we consider each of the constituent distributions in Equation (37). As mentioned in Section 3.2, the *measurement distribution* is Gaussian distributed, which can be rearranged such that the mean of the distribution is the observation

$$\begin{aligned} p(\mathbf{z}_i = \mathbf{z}_i | \mathbf{m}_i) & = \mathcal{N}_m(\mathbf{z}_i = \mathbf{z}_i; \mathbf{m}_i, \boldsymbol{\Sigma}_{\mathbf{z}_i}) \\ & = \mathcal{N}_m(\mathbf{m}_i; \mathbf{z}_i, \boldsymbol{\Sigma}_{\mathbf{z}_i}). \end{aligned} \quad (39)$$

According to the surfel model in Section 4, the *likelihood distribution* is Gaussian distributed

$$p(\gamma_i|\alpha_i, \beta_i, \mathbf{h}, \nu_{\mathcal{B}}) = \mathcal{N}_m(\gamma_i; f(\mathbf{h}, \alpha_i, \beta_i), \nu_{\mathcal{B}}), \quad (40)$$

where $f(\cdot)$ is the mean of the stochastic process as defined in Equation (9). We place an uninformative and independently distributed Gaussian prior over α_i and β_i , and combine it with $\tilde{\delta}_{i\leftarrow}(\mathbf{h})$ to form the jointly Gaussian distributed *context distribution*

$$p(\alpha_i)p(\beta_i)\tilde{\delta}_{i\leftarrow}(\mathbf{h}) = \mathcal{N}_m([\mathbf{h} \ \alpha_i \ \beta_i]^\top; \boldsymbol{\mu}_c, \boldsymbol{\Sigma}_c), \quad (41)$$

with moments calculated as

$$\boldsymbol{\mu}_c = \begin{bmatrix} \boldsymbol{\mu}_{i\leftarrow} \\ \mu_{\alpha_i} \\ \mu_{\beta_i} \end{bmatrix} \quad \text{and} \quad \boldsymbol{\Sigma}_c = \text{diag}(\boldsymbol{\Sigma}_{i\leftarrow}, \sigma_{\alpha_i}^2, \sigma_{\beta_i}^2), \quad (42)$$

where $\boldsymbol{\Sigma}_{i\leftarrow} = \boldsymbol{\Omega}_{i\leftarrow}^{-1}$, $\boldsymbol{\mu}_{i\leftarrow} = \boldsymbol{\Sigma}_{i\leftarrow}\boldsymbol{\xi}_{i\leftarrow}$, and the $\text{diag}(\cdot)$ operator creates a block diagonal matrix of its arguments. Most notably, all distributions except the likelihood distribution are exactly Gaussian distributed over \mathbf{h} and \mathbf{m}_i . This dissimilarity in likelihood distribution is due to the nonlinear relationships introduced by $f(\cdot)$. To ensure that the product of all the distributions is tractable, we also wish to approximate the likelihood distribution as a Gaussian distribution. A common approach to achieving is by linearising; we therefore use a linear Taylor series approximation

$$f(\mathbf{x}) \approx f(\bar{\mathbf{x}}) + \mathbf{F}(\mathbf{x} - \bar{\mathbf{x}}), \quad (43)$$

where $\mathbf{x} = [\mathbf{h} \ \alpha_i \ \beta_i]^\top$, and \mathbf{F} is the Jacobian matrix of $f(\mathbf{x})$ evaluated at the linearisation point $\boldsymbol{\mu}_c$

$$\begin{aligned} \mathbf{F} &= \left. \frac{\delta f}{\delta \mathbf{x}} \right|_{\mathbf{x}=\boldsymbol{\mu}_c} \\ &= \left[1 - \alpha_i - \beta_i \quad \alpha_i \quad \beta_i \quad h_\alpha - h_0 \quad h_\beta - h_0 \right] \Big|_{\boldsymbol{\mu}_c}. \end{aligned} \quad (44)$$

Using this we can calculate the product of the likelihood and context distributions

$$\begin{aligned} &p(\gamma_i|\alpha_i, \beta_i, \mathbf{h}, \nu_{\mathcal{B}})p(\alpha_i)p(\beta_i)\tilde{\delta}_{i\leftarrow}(\mathbf{h}) \\ &\propto \mathcal{N}_c([\mathbf{h} \ \mathbf{m}_i]^\top; \bar{\boldsymbol{\xi}}, \bar{\boldsymbol{\Omega}}), \end{aligned} \quad (45)$$

with natural parameters calculated as

$$\bar{\boldsymbol{\xi}} = \bar{\boldsymbol{\Omega}} \begin{bmatrix} \boldsymbol{\mu}_c \\ f(\boldsymbol{\mu}_c) \end{bmatrix} \quad \text{and} \quad \bar{\boldsymbol{\Omega}} = \begin{bmatrix} \boldsymbol{\Sigma}_c & (\mathbf{F}\boldsymbol{\Sigma}_c)^\top \\ \mathbf{F}\boldsymbol{\Sigma}_c & \mathbf{F}\boldsymbol{\Sigma}_c\mathbf{F}^\top + \nu_{\mathcal{B}} \end{bmatrix}^{-1}. \quad (46)$$

The normalised product of the prediction distribution and the measurement distribution results in the desired belief

$$\tilde{\mathcal{B}}(\mathbf{h}, \mathbf{m}_i) = \mathcal{N}_c([\mathbf{h} \ \mathbf{m}_i]^\top; \boldsymbol{\xi}, \boldsymbol{\Omega}), \quad (47)$$

with natural parameters calculated as

$$\begin{aligned} \boldsymbol{\xi} &= \bar{\boldsymbol{\xi}} + \mathbf{S}^\top \boldsymbol{\Sigma}_{z_i}^{-1} \mathbf{z}_i & \boldsymbol{\Omega} &= \bar{\boldsymbol{\Omega}} + \mathbf{S}^\top \boldsymbol{\Sigma}_{z_i}^{-1} \mathbf{S} \\ &= \begin{bmatrix} \boldsymbol{\xi}_h \\ \boldsymbol{\xi}_m \end{bmatrix} & \text{and} & &= \begin{bmatrix} \boldsymbol{\Omega}_{hh} & \boldsymbol{\Omega}_{hm} \\ \boldsymbol{\Omega}_{mh} & \boldsymbol{\Omega}_{mm} \end{bmatrix}, \end{aligned} \quad (48)$$

where $\mathbf{S} = [\mathbf{0}_{3 \times 3} \quad \mathbf{I}_{3 \times 3}]$ is a selection matrix. Notably, the above method is equivalent to an extended information filter (EIF) with a nonlinear state transition model and a linear measurement model [59, ch. 3.5.4]. Finally, we can calculate $\tilde{\phi}_l(\mathbf{h}, \mathbf{m}_i)$ by dividing out $\tilde{\delta}_{i\leftarrow}(\mathbf{h})$ from $\tilde{\mathcal{B}}(\mathbf{h}, \mathbf{m}_i)$ (Equation (36)) which results in

$$\tilde{\phi}_l(\mathbf{h}, \mathbf{m}_i) = \mathcal{N}_c([\mathbf{h} \ \mathbf{m}_i]^\top; \boldsymbol{\xi}_l, \boldsymbol{\Omega}_l), \quad (49)$$

with natural parameters calculated as

$$\boldsymbol{\xi}_l = \begin{bmatrix} \boldsymbol{\xi}_h - \boldsymbol{\xi}_{i\leftarrow} \\ \boldsymbol{\xi}_m \end{bmatrix} \quad \text{and} \quad \boldsymbol{\Omega}_l = \begin{bmatrix} \boldsymbol{\Omega}_{hh} - \boldsymbol{\Omega}_{i\leftarrow} & \boldsymbol{\Omega}_{hm} \\ \boldsymbol{\Omega}_{mh} & \boldsymbol{\Omega}_{mm} \end{bmatrix}. \quad (50)$$

From this result, we can now calculate a part of the outgoing message, $\tilde{\delta}_{i\rightarrow}(\mathbf{h})$, by marginalising out \mathbf{m}_i . Therefore, using Equation (16), we can calculate the natural parameters of $\tilde{\delta}_{i\rightarrow}(\mathbf{h})$ (Equation (27)) as

$$\boldsymbol{\Omega}_{i\rightarrow} = \boldsymbol{\Omega}_{hh} - \boldsymbol{\Omega}_{j\leftarrow} - \boldsymbol{\Omega}_{hm} \boldsymbol{\Omega}_{mm}^{-1} \boldsymbol{\Omega}_{mh} \quad (51)$$

and

$$\boldsymbol{\xi}_{i\rightarrow} = \boldsymbol{\xi}_h - \boldsymbol{\xi}_{j\leftarrow} - \boldsymbol{\Omega}_{hm} \boldsymbol{\Omega}_{mm}^{-1} \boldsymbol{\xi}_m. \quad (52)$$

We have now discussed how to calculate the likelihood cluster potential $\tilde{\phi}_l(\mathbf{h}, \mathbf{m}_i)$ and the outgoing message $\tilde{\delta}_{i\rightarrow}(\mathbf{h})$. Next we focus on the likelihood cluster potential and outgoing message over the planar deviation.

5.1.2. Updating Planar Deviation Factor

Similarly to calculating $\tilde{\phi}_l(\mathbf{h}, \mathbf{m}_i)$, to perform the local information projection of Equation (22) with respect to $\tilde{\phi}_l(\nu)$, the VMP algorithm [55] defines the iterative update as

$$\begin{aligned} & \log \tilde{\phi}_l(\nu) + \log \tilde{\delta}_{i\leftarrow}(\nu) \\ & \propto \left\langle \log \phi_l(\boldsymbol{\theta}, \mathbf{m}_i, \mathbf{z}_i = \mathbf{z}_i) \tilde{\delta}_{i\leftarrow}(\boldsymbol{\theta}) \right\rangle_{\tilde{\mathcal{B}}(\mathbf{h}, \mathbf{m}_i)}. \end{aligned} \quad (53)$$

The marginalisation to calculate the outgoing message $\tilde{\delta}_{i\rightarrow}(\boldsymbol{\theta})$ —Equation (16)—will have no effect on the outgoing message $\tilde{\delta}_{i\rightarrow}(\nu)$ due to our choice of factorisation. Therefore, solving for the cluster potential is equivalent to solving for the outgoing message— $\tilde{\delta}_{i\rightarrow}(\nu) = \tilde{\phi}_l(\nu)$ —which we can directly calculate as

$$\begin{aligned} \log \tilde{\delta}_{i\rightarrow}(\nu) & \propto \left\langle \log p(\gamma_i | \alpha_i, \beta_i, \mathbf{h}, \nu) \right\rangle_{\tilde{\mathcal{B}}(\mathbf{h}, \mathbf{m}_i)} \\ & \propto -a_{i\rightarrow} \log \nu - \frac{b_{i\rightarrow}}{\nu}, \end{aligned} \quad (54)$$

where $\tilde{\mathcal{B}}(\mathbf{h}, \mathbf{m}_i)$ is calculated from Equation (37). The resulting approximate potential matches the form of an inverse-gamma distribution with scale and shape parameters

$$a_{i\rightarrow} = \frac{1}{2} \quad \text{and} \quad b_{i\rightarrow} = \frac{1}{2} \left\langle (\gamma_i - f(\alpha_i, \beta_i, \mathbf{h}))^2 \right\rangle_{\tilde{\mathcal{B}}(\mathbf{h}, \mathbf{m}_i)}, \quad (55)$$

where $f(\cdot)$ is defined by Equation (9). We again use the linear Taylor series approximation to calculate the expectation¹⁴, where we linearise around the mean of $\tilde{\mathcal{B}}(\mathbf{h}, \mathbf{m}_i)$. This results in the expectation

$$b_{i\rightarrow} = \frac{1}{2} \mathbf{F}_{\text{aug}} \boldsymbol{\Sigma} \mathbf{F}_{\text{aug}}^\top + \frac{1}{2} (\mu_\gamma - f(\mu_\alpha, \mu_\beta, \boldsymbol{\mu}_h))^2, \quad (56)$$

where $\mathbf{F}_{\text{aug}} = [\mathbf{F} \quad \mathbf{1}]$ —with \mathbf{F} defined by Equation (44)—and $\boldsymbol{\Sigma} = \boldsymbol{\Omega}^{-1}$ and $\boldsymbol{\mu} = \boldsymbol{\Sigma} \boldsymbol{\xi}$ are the moments of the distribution in Equation (47).

We have now discussed how to perform inference on each surfel in isolation. Before discussing performing inference on the full model, we will briefly look at the performance of the proposed inference algorithm.

¹⁴ This expectation could be calculated analytically, because $f(\cdot)$ is a multilinear function and $\tilde{\mathcal{B}}(\mathbf{h}, \mathbf{m}_i)$ is Gaussian distributed. However, we found that in rare cases it was problematic for the initially uncertain stages of message passing, and consequently hindered convergence. In contrast, using the Taylor series approximation was found to be a more robust approach. Additionally, the Taylor series is computationally cheaper to compute.

5.1.3. Inference Performance

To illustrate the performance of the proposed inference algorithm, we compare our approximation of the surfel model belief against Markov chain Monte Carlo (MCMC) samples of the exact belief distribution for a 2-D simulation—using the Metropolis-Hastings algorithm to generate samples. Figure 9 shows representative cases for a stereo camera and a LiDAR sensor. We see that our algorithm accurately matches with the marginal distributions from MCMC. In cases where the measurement uncertainty is unreasonably high¹⁵, our algorithm results can differ noticeably with the exact belief; this is due to errors induced through linearisation. However, when more measurements are added, this effect is mitigated. We also did not encounter any issues with this when using either simulation or practical data—as we will see in Section 6.

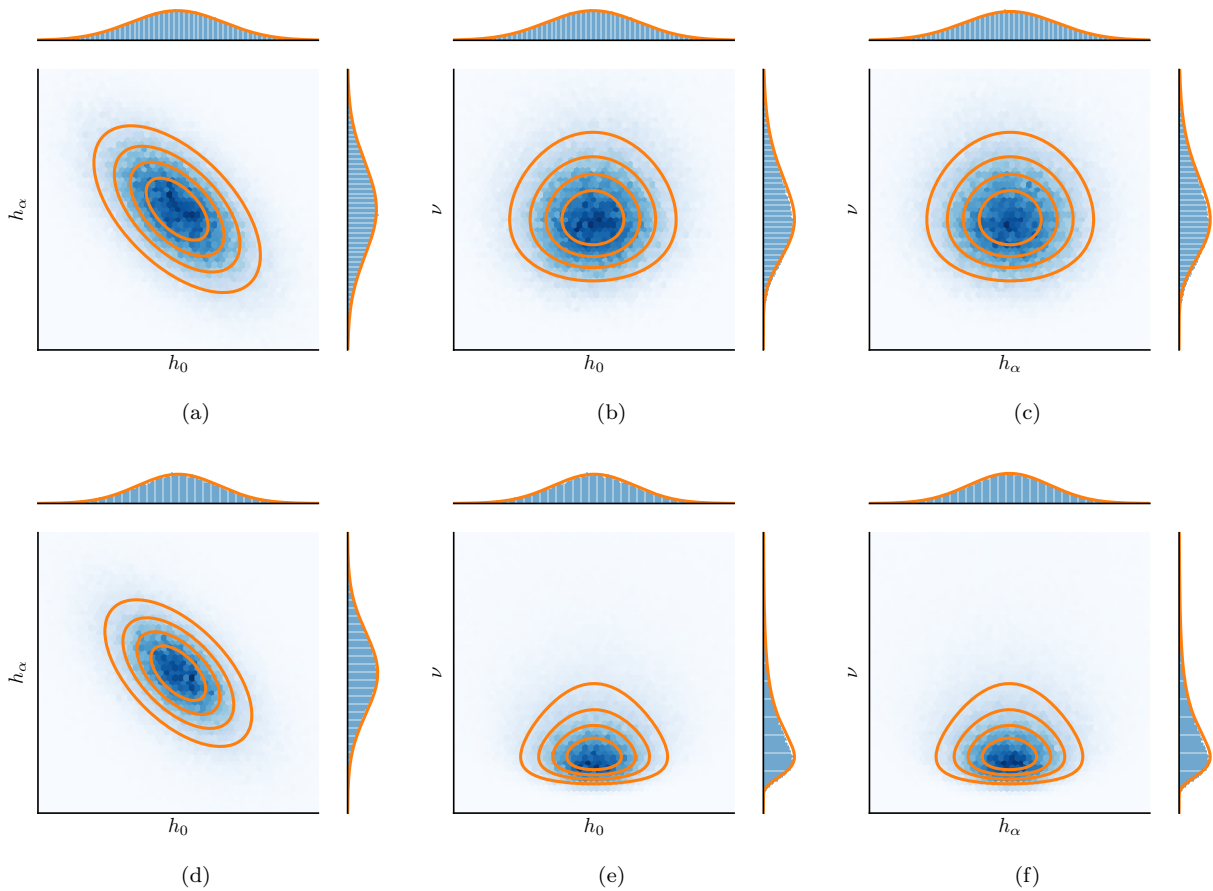


Figure 9: The accuracy of our inference algorithm in calculating an approximate surfel model belief (orange), compared against MCMC samples of the exact belief distribution (blue) for a 2-D simulation. We emulate two different sensor modalities: (a-c) a stereo camera by using 100 measurements with high range and low bearing uncertainty, and (d-f) a LiDAR sensor by using 10 measurements with low measurement uncertainty. Shown for these two cases are the three 2-D projections of the 3-D belief distribution over h_0 , h_α , and ν , and the marginal distributions for each axis. Note that we do not show the axes ticks as we are only concerned with the *relative* difference between the exact belief with our approximation.

We have shown that this method of approximation can accurately represent the surfel belief; however,

¹⁵The measurement uncertainty relative to the size of the grid element increases with the grid division depth. Therefore, too fine a grid division could result in a measurement distribution which spans over several grid elements.

this was only for the case where each surfel is updated in isolation. We will now consider inference on the full model, utilising the approach we have developed here.

5.2. Inference on the Full Model

As opposed to calculating the joint belief distribution over all the surfel parameters in a STM map, we instead wish to calculate the marginal belief distributions over each surfel’s parameters. However, as there are shared height parameters between contiguous surfels, we cannot naively use exactly the same approach as we did previously to perform inference on the full model. It should be noted that although we will consider the joint distribution over all the map parameters, we do not expressly calculate this, as the marginal surfel beliefs are our desired end result.

We can reformulate the inference problem over all the map parameters by utilising our previous approach of performing independent surfel inference. For a given surfel, s , we assume that measurements within the associated grid element, Z_s , and the points on the surface of the environment, M_s , are independent of all other measurements, $Z \setminus Z_s$, and all other surface points, $M \setminus M_s$, given the parameters of the surfel, θ_s . Following this assumption, and using Bayes’ theorem, we can factorise the full joint distribution

$$\begin{aligned} p(\Theta, M, Z) &= p(\Theta)p(M, Z|\Theta) \\ &= p(\Theta) \prod_{s \in S} p(M_s, Z_s|\theta_s), \end{aligned} \quad (57)$$

where S is the set of all surfels in a STM map. Each conditional distribution, $p(M_s, Z_s|\theta_s)$, is described by the same model we used previously, namely

$$p(M_s, Z_s|\theta_s) = \prod_i \phi_l(\theta_s, \mathbf{m}_i, \mathbf{z}_i), \quad (58)$$

where we again refer to $\phi_l(\theta_s, \mathbf{m}_i, \mathbf{z}_i)$ as the likelihood cluster potential—as defined in Equations (13) and (14). We factorise the prior distribution into a product of prior cluster potentials

$$p(\Theta) \propto \prod_{s \in S} \phi_p(\theta_s). \quad (59)$$

As with our previous approach, each prior cluster potential is distributed according to Equation (28)—namely a Gaussian distribution over the vertex heights and an inverse-gamma distribution over the planar deviation. We will look into the effect that this factorisation has on the resulting surfel beliefs, and how the parameter choices (specifically for the height prior distribution) could encode additional structure in the environment (Section 6.1). Combining the prior factorisation with Equation (58), we obtain

$$p(\Theta, M, Z) = \prod_{s \in S} \phi_s(\theta_s, M_s, Z_s), \quad (60)$$

where the surfel cluster potential, $\phi_s(\theta_s, M_s, Z_s)$, is calculated according to

$$\begin{aligned} \phi_s(\theta_s, M_s, Z_s) &= \phi_p(\theta_s)p(M_s, Z_s|\theta_s) \\ &= \phi_p(\theta_s) \prod_i \phi_l(\theta_s, \mathbf{m}_i, \mathbf{z}_i). \end{aligned} \quad (61)$$

For notational brevity we drop the (observed) measurements from each surfel cluster potential

$$\phi_s(\theta_s, M_s) \triangleq \phi_s(\theta_s, M_s, Z_s = \mathbf{Z}_s). \quad (62)$$

To calculate a surfel belief for some given measurements, $Z = \mathbf{Z}$, we must marginalise out $\setminus \boldsymbol{\theta}_s$ —all variables except for $\boldsymbol{\theta}_s$ —from the full joint distribution

$$\begin{aligned} \mathcal{B}(\boldsymbol{\theta}_s) &\propto \int_{\setminus \boldsymbol{\theta}_s} p(\boldsymbol{\theta}, M, Z = \mathbf{Z}) \, d \setminus \boldsymbol{\theta}_s \\ &= \int_{\setminus \boldsymbol{\theta}_s} \prod_{s \in S} \phi_s(\boldsymbol{\theta}_s, M_s) \, d \setminus \boldsymbol{\theta}_s. \end{aligned} \quad (63)$$

The surfel belief can be separated into two terms: one containing the surfel cluster potential of a surfel, $s \in S$, and the other containing the surfel cluster potentials of the rest of surfels, $R = S \setminus s$, namely

$$\begin{aligned} \mathcal{B}(\boldsymbol{\theta}_s) &\propto \underbrace{\int_{M_s} \phi_s(\boldsymbol{\theta}_s, M_s) \, dM_s}_{\phi_p(\boldsymbol{\theta}_s) \prod_i \delta_{i \rightarrow s}(\boldsymbol{\theta}_s)} \underbrace{\int_{\setminus \boldsymbol{\theta}_s} \prod_{r \in R} \phi_r(\boldsymbol{\theta}_r, M_r) \, d \setminus \boldsymbol{\theta}_s}_{\delta_{s \leftarrow R}(\mathbf{h}_s)}. \end{aligned} \quad (64)$$

The first factor is identical to what was calculated previously when considering each surfel in isolation, with the messages from each likelihood cluster calculated according to Equation (16). For now we will assume that we can calculate this term. The second term is the message from the rest of the surfels in the map, which is due to the shared heights between surfels. This message essentially captures what the rest of the surfels in the map surmise about the heights of the current surfel. Because of the highly coupled nature of the problem, the marginalisation to calculate $\delta_{s \leftarrow R}(\mathbf{h}_s)$ is expensive to compute. To keep things tractable, we approximate this message using a technique known as loopy belief propagation (LBP) [60]—a message passing technique that is particularly well suited to calculating approximate marginal distributions without expressly calculating the full joint distribution. LBP is an iterative application of the integral-product algorithm applied to loopy networks.

In order use LBP, we must first construct a cluster graph for the full inference problem. We previously performed inference by only considering each surfel cluster potential when calculating each surfel belief in isolation. We can therefore construct the cluster graph of the full joint distribution, $p(\boldsymbol{\theta}, M, Z)$, by repeating the previous cluster graph (Figure 8c) for each surfel in the map, but also creating connections between surfels that share an edge. The resulting cluster graph is illustrated in Figure 10. The scope of the sepset between surfels is generally over the two heights from shared edge between the surfels—for example $\mathcal{S}_{s,a} = \mathbf{h}_s \cap \mathbf{h}_a$. Although it is not explicitly shown, to ensure a valid cluster graph of the joint distribution, it is also necessary to reduce the scope of some sepsets so that the graph obeys the *running intersection property*, which states that there can only be a single path between the same variable in different parts of the graph.

From this cluster graph, we can instead calculate an approximation to the message from the rest of the surfels in the map, $\tilde{\delta}_{s \leftarrow R}(\mathbf{h}_s)$, by only considering the messages from the subset of surfels that are contiguous to the current surfel, $C \subset R$. This results in a much simpler and tractable calculation

$$\tilde{\delta}_{s \leftarrow R}(\mathbf{h}_s) \propto \prod_{c \in C} \delta_{s \leftarrow c}(\mathcal{S}_{s,c}), \quad (65)$$

where \mathcal{S} denotes the sepset between surfels. It should be noted that the resulting message scope might not always contain all the heights in the surfel (as would be the case for surfels on the border of the submap, or if the sepset scope has been reduced to satisfy the running intersection property). Using the integral-product algorithm, LBP defines the iterative update of a message from one surfel, s , to another surfel, a , according

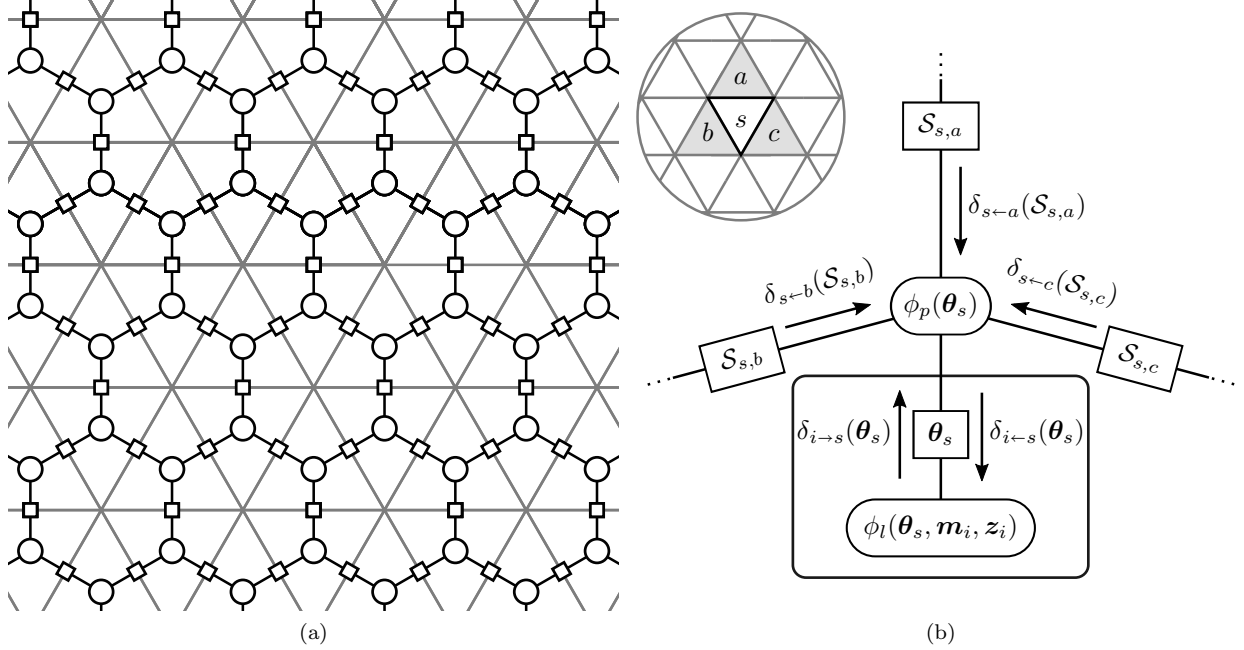


Figure 10: (a) The cluster graph for the full inference problem shown for a zoomed-in section of a stochastic triangular mesh (STM) map. We indicate the sepsets between clusters with \square , and each surfel cluster potential with \circ . The grey lines indicate the grid elements of the map. (b) We zoom into the cluster graph, focusing on a specific surfel, s , which is contiguous with surfels a , b and c . The resulting graph is similar to the cluster graph in Figure 8c, but there are now connections between contiguous surfels. The sepset between the surfels is denoted \mathcal{S} (see text for more details on the scope of the sepsets).

to

$$\begin{aligned} & \delta_{a \leftarrow s}(\mathcal{S}_{a,s}) \\ & \propto \int_{\setminus \mathcal{S}_{a,s}} \phi_p(\boldsymbol{\theta}_s) \prod_i \delta_{i \rightarrow s}(\boldsymbol{\theta}_s) \prod_{c \in C \setminus a} \delta_{s \leftarrow c}(\mathcal{S}_{s,c}) d \setminus \mathcal{S}_{a,s}. \end{aligned} \quad (66)$$

Using Equation (64), this can be simplified to

$$\delta_{a \leftarrow s}(\mathcal{S}_{a,s}) \propto \int_{\setminus \mathcal{S}_{a,s}} \frac{\mathcal{B}(\boldsymbol{\theta}_s)}{\delta_{s \leftarrow a}(\mathcal{S}_{a,s})} d \setminus \mathcal{S}_{a,s}. \quad (67)$$

By iteratively passing these messages between surfels, LBP approximately calculates the marginal belief of each surfel. In order to perform this marginalisation and calculate each surfel belief, the likelihood cluster potentials in each surfel potential need to have a closed-form solution, but this is not the case due to the nonlinearities between the variables in the likelihood cluster potentials. In order to find a closed-form solution to each surfel belief (and consequently the map belief) we again turn to variational message passing (VMP) to approximate each likelihood cluster potential; that is, using the local information projection according to Equation (22), repeated here for clarity

$$\hat{\phi}_l^*(\boldsymbol{\theta}_s, \mathbf{m}_i) = \arg \min_{\hat{\phi}_l \in \mathcal{F}} D_{\text{KL}} \left(\hat{\phi}_l \tilde{\delta}_{i \leftarrow s} \parallel \phi_l \tilde{\delta}_{i \leftarrow s} \right).$$

However, the approximate incoming message, $\tilde{\delta}_{i \leftarrow s}(\boldsymbol{\theta}_s)$, is now calculated according to

$$\tilde{\delta}_{i \leftarrow s}(\boldsymbol{\theta}_s) = \phi_p(\boldsymbol{\theta}_s) \tilde{\delta}_{s \leftarrow R}(\mathbf{h}_s) \prod_{j \neq i} \tilde{\delta}_{j \rightarrow s}(\boldsymbol{\theta}_s). \quad (68)$$

Similarly to previously—Equation (17)—this message is calculated by combining the prior cluster potential, $\phi_p(\boldsymbol{\theta}_s)$, with the messages from all other likelihood clusters, $\prod_{j \neq i} \tilde{\delta}_{j \rightarrow s}(\boldsymbol{\theta}_s)$, but now additionally combines the message from neighbouring surfels, $\tilde{\delta}_{s \leftarrow R}(\mathbf{h}_s)$. Using Equation (64), the approximate incoming message can be rewritten in terms of the surfel belief

$$\tilde{\delta}_{i \leftarrow s}(\boldsymbol{\theta}_s) \propto \frac{\tilde{\mathcal{B}}(\boldsymbol{\theta}_s)}{\tilde{\delta}_{i \rightarrow s}(\boldsymbol{\theta}_s)}, \quad (69)$$

which, in comparison to Equation (68), is cheaper to calculate when iterating over all the measurements. If we combine the prior potential, $\phi_p(\boldsymbol{\theta}_s)$, with the incoming message, $\tilde{\delta}_{s \leftarrow R}(\mathbf{h}_s)$, into a pseudo-prior, the same approach to what we described previously can be used to perform the local information projection. This specifically includes using the Gaussian family of distributions to model the height distributions, which results in LBP performing approximate inference on only Gaussian distributions—a variant of LBP known as Gaussian LBP. Gaussian LBP is a standard problem formulation for which there are implementations available, and we therefore use an in-house PGM library¹⁶. LBP is a tractable approximate inference technique; however, due to its iterative nature, its convergence has not yet been proven. In Gaussian LBP, however, it is known that if convergence is reached, the posterior means are correct [61, 62]. Although the surfel belief distributions in our problem are not guaranteed to be exactly Gaussian, as the number of measurements becomes large enough, this is a fair assumption. In our implementation we have also not empirically experienced any issues with convergence.

The approach presented here performs inference on a STM map using a hybrid message passing technique using loopy belief propagation (LBP) and variational message passing (VMP). Next we will provide an overview of the proposed inference algorithm, and discuss some aspects of its implementation.

5.3. Algorithm Overview and Implementation

In Algorithm 1 we describe the process of performing inference given a single batch of measurements—this could be a batch of measurements accumulated over time, or from a single time-step. Notably, lines 7 to 9 and 16 to 18 correspond to the loopy belief propagation (LBP) update steps, and lines 10 to 15 to the variational message passing (VMP) update steps. We also adjust the method of updating each surfel belief to be more efficient: if only the incoming message from neighbouring surfels has changed during the iterative update process, then it is unnecessary to calculate the updated surfel belief using Equation (64). We instead (equivalently) simplify the update to

$$\tilde{\mathcal{B}}(\boldsymbol{\theta}_s) \triangleq \tilde{\mathcal{B}}(\boldsymbol{\theta}_s) \frac{\tilde{\delta}_{s \leftarrow R}^*(\mathbf{h}_s)}{\tilde{\delta}_{s \leftarrow R}(\mathbf{h}_s)} \quad (70)$$

where we denote the updated and previous incoming messages $\tilde{\delta}_{s \leftarrow R}^*$ and $\tilde{\delta}_{s \leftarrow R}$, respectively. We will now discuss some of the aspects of the algorithm.

Message Initialisation. We first need to initialise all of the messages before we can begin message passing. In general, the initialisation for iterative approximate inference algorithms can influence the performance, affecting the local optimum to which the algorithm converges and the convergence speed. We initialise the messages between surfels to be vacuous. For the outgoing messages from each likelihood cluster, we use a simple empirical method of initialisation. Specifically, we initialise each outgoing message $\tilde{\delta}_{i \rightarrow s}(\mathbf{h}_s)$ to have a mean at the γ component of the measurement \mathbf{z}_i and a (practically) uninformative covariance. This ensures that $\tilde{\mathcal{B}}(\mathbf{h})$ is initialised to have a mean at the average γ component of the measurements. We initialise each outgoing message $\tilde{\delta}_{i \rightarrow s}(\nu_s)$ such that expected value calculated in Equation (38) is the variance of the γ component of the measurements.

¹⁶This is currently in the process of being made open-source.

Algorithm 1 STM Map Inference

Inputs:
 Prior cluster potentials for each surfel: $\phi_p(\boldsymbol{\theta}_s) \forall s \in S$
 Measurements in each surfel: $\mathbf{Z}_s \forall s \in S$

Output:
 Surfel beliefs: $\tilde{\mathcal{B}}(\boldsymbol{\theta}_s) \forall s \in S$

- 1: Initialise all messages
- ▷ *Initialise all surfel beliefs* Equation (64)
- 2: **for all** $s \in S$ **do**
- 3: $\tilde{\mathcal{B}}(\boldsymbol{\theta}_s) \leftarrow \phi_p(\boldsymbol{\theta}_s) \tilde{\delta}_{s \leftarrow R}(\mathbf{h}_s) \prod_i \tilde{\delta}_{i \rightarrow s}(\boldsymbol{\theta}_s)$
- 4: **end for**
- 5: **repeat**
- ▷ *Cycle through all the surfels in the map*
- 6: **for all** $s \in S$ **do**
- ▷ *Calculate the updated incoming message from neighbouring surfels* Equation (65)
- 7: $\tilde{\delta}_{s \leftarrow R}^*(\mathbf{h}_s) \leftarrow \prod_{c \in C} \delta_{s \leftarrow c}(\mathcal{S}_{s,c})$
- ▷ *Update the surfel belief* Equation (70)
- 8: $\tilde{\mathcal{B}}(\boldsymbol{\theta}_s) \leftarrow \tilde{\mathcal{B}}(\boldsymbol{\theta}_s) \frac{\tilde{\delta}_{s \leftarrow R}^*(\mathbf{h}_s)}{\tilde{\delta}_{s \leftarrow R}(\mathbf{h}_s)}$
- 9: $\tilde{\delta}_{s \leftarrow R}(\mathbf{h}_s) \leftarrow \tilde{\delta}_{s \leftarrow R}^*(\mathbf{h}_s)$
- ▷ *Update the likelihood cluster potential for each measurement*
- 10: **for all** $\mathbf{z}_i \in \mathbf{Z}_s$ **do**
- ▷ *Calculate incoming message to the likelihood cluster* Equation (69)
- 11: $\tilde{\delta}_{i \leftarrow s}(\boldsymbol{\theta}_s) \leftarrow \frac{\tilde{\mathcal{B}}(\boldsymbol{\theta}_s)}{\tilde{\delta}_{i \rightarrow s}(\boldsymbol{\theta}_s)}$
- ▷ *Update the likelihood cluster potential* Sections 5.1.1 and 5.1.2
- 12: $\tilde{\phi}_l(\mathbf{h}, \mathbf{m}_i) \tilde{\phi}_l(\nu) \leftarrow \arg \min_{\tilde{\phi}_l} D_{\text{KL}} \left(\tilde{\phi}_l \tilde{\delta}_{i \leftarrow s} \parallel \phi_l \tilde{\delta}_{i \leftarrow s} \right)$
- ▷ *Calculate the outgoing message from the likelihood cluster* Equation (16)
- 13: $\tilde{\delta}_{i \rightarrow s}(\boldsymbol{\theta}_s) \leftarrow \tilde{\phi}_l(\nu) \int \phi_l(\mathbf{h}, \mathbf{m}_i) d\mathbf{m}_i$
- ▷ *Update the surfel belief* Equation (21)
- 14: $\tilde{\mathcal{B}}(\boldsymbol{\theta}_s) \leftarrow \tilde{\delta}_{i \rightarrow s}(\boldsymbol{\theta}_s) \tilde{\delta}_{i \leftarrow s}(\boldsymbol{\theta}_s)$
- 15: **end for**
- ▷ *Calculate the outgoing messages to neighbouring surfels* Equation (67)
- 16: **for all** $c \in C$ **do**
- 17: $\delta_{c \leftarrow s}(\mathcal{S}_{c,s}) = \int \frac{\mathcal{B}(\boldsymbol{\theta}_s)}{\tilde{\delta}_{s \leftarrow c}(\mathcal{S}_{c,s})} d \setminus \mathcal{S}_{c,s}$
- 18: **end for**
- 19: **end for**
- 20: **until** all messages converge

Incremental Updating. During online operation, measurements are received incrementally, and we wish to calculate the surfel beliefs based on all currently available measurements. Ideally, the surfel beliefs should be recalculated as new measurement batches arrive while also considering all previous measurements. However,

as more measurement batches are received, this approach would quickly become intractable. A viable approximation is to only update the outgoing messages from a window of the W latest measurements [63]. Fixing the messages from clusters containing measurements outside this window ensures that updating the surfel belief is linear in the window size W . In practice, we combine these constant messages with the prior, discarding the old measurements so that the storage will not grow unbounded. This new prior now summarises all the previous measurements. Following this approach, we can then use the same procedure outlined in Algorithm 1. It should also be noted that previously calculated messages between surfels should not be discarded, but now used as the initialisation for the next batch update.

Convergence. To monitor the state of convergence, we use the fact that at convergence all messages will be constant—that is, convergence has been reached if all messages do not change between iterations. In practice, a message is deemed to be constant if the difference between the message successive iterations is negligible. To evaluate this difference we use the exclusive Kullback-Leibler (KL) divergence¹⁷ between a message at the current and previous iterations— D_{KL} (current iteration \parallel previous iteration)—and the message has converged if the resulting divergence is below a threshold. If all messages related to a surfel have converged, then it is no longer necessary to iterate over it. It should also be noted that although convergence is not theoretically guaranteed (due to the use of loopy belief propagation (LBP)), we have not empirically experienced any issues with convergence with our implementation.

Computational Complexity. We can see that the asymptotic computational complexity of our algorithm is $\mathcal{O}(KN)$, where K is the number of iterations in the outermost loop before convergence and N is the total number of measurements being incorporated into the map. In practice, K is constant with respect to N , and therefore the algorithm can be considered approximately linear in N . We support this claim with experimental results (Section 6.2).

We have now described performing inference on a STM map. Next we will look at a series of experiments evaluating the use a STM map to represent environments on both simulated and practical data.

6. Experimental Results

Up to this point we have discussed how a STM map models the environment, as well as the process of performing inference in the map. We now investigate how the STM mapping technique performs under different experimental conditions.

For the first set of experiments, we use simulated measurement data (Sections 6.1 to 6.3). We look at how the prior distribution parameter choices affect the resulting map (Section 6.1), analyse the cost of performing inference (Section 6.2), and compare the accuracy of a STM map at modelling an environment to an elevation map (Section 6.3). We then consider practical datasets collected using first stereo cameras and then a LiDAR sensor (Sections 6.4 and 6.5, respectively). We demonstrate the modelling performance of the STM mapping technique in relative and global inertial reference frames (IRFs), and perform a qualitative analysis of the resulting STM maps (Sections 6.4 and 6.5, respectively).

6.1. Parameters of the Prior Distribution

In Section 5.1 we gave the form of the prior distribution over the surfel parameters—Equation (28)—but did not specify the parameters of the prior distribution. For surfels in the map that contains many measurements, the choice of prior parameters has a negligible effect on the resulting map belief. However, if there are clusters of neighbouring surfels with no measurements, then these surfels’ beliefs are largely determined by the respective prior distributions.

We want to capture knowledge of the structure of the environment in the prior distribution. The structure we expect is that neighbouring regions tend to have similar heights, which means that we expect

¹⁷However, other divergences could be used: the symmetric KL divergence, inclusive KL divergence, the Mahalanobis distance, or the Bhattacharyya distance to name a few.

neighbouring heights to be positively correlated. If a completely uninformative height prior distribution is used, then only the heights of shared vertices will be affected when performing inference in unobserved regions. In order to achieve this we use a height prior distribution with covariance

$$\Sigma_p = \sigma^2 \begin{bmatrix} 1 & \rho & \rho \\ \rho & 1 & \rho \\ \rho & \rho & 1 \end{bmatrix} \quad (71)$$

where ρ is the Pearson correlation coefficient and σ^2 the variance. Without any other information, we expect the heights in a submap to be distributed around the submap plane. We therefore choose the mean of the height prior distribution to represent this initial belief; that is, we set the mean to the zero vector. We choose σ^2 to be uninformative and focus on ρ , which should be chosen in the range $\rho \in [0, 1)$ to ensure a positively correlated prior distribution. It should be noted that as the planar deviations in neighbouring surfels are modelled as being statically independent, we model the prior of the planar deviation in a surfel as an uninformative inverse-gamma distribution.

In Figure 11 we show the result of varying the correlation coefficient on the map belief for a 2-D simulation. From this we can see that by increasing the correlation coefficient, the mean heights of unobserved surfels are affected at an increasing distance from the observed region, which is consistent with smoothly varying environments. We empirically chose $\rho = 0.5$, although this choice may vary depending on the nature of the environment. This parameter could conceivably be learnt from data.

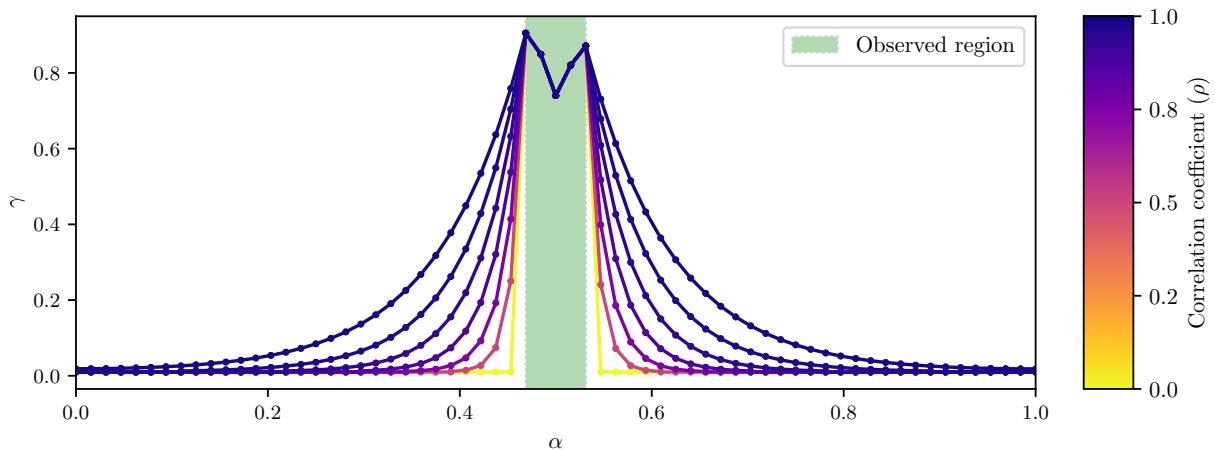


Figure 11: The effect of using a correlated prior distribution when a section of the environment is observed. This is shown for a series of correlation coefficients, spaced using a geometric series: $\{0, 2^{-1}, 2^{-1} + 2^{-2}, \dots\}$. Only the mean of the mean mesh belief is shown, and is coloured according to the correlation coefficient (the darker, the more correlated).

6.2. Cost of Inference

From a tractability perspective, for the STM mapping technique to be viable for online dense mapping, the cost of incorporating one measurement into the map should be constant irrespective of the size of the map or the number of measurements in the map. This computational requirement is equivalent to the computational complexity of updating the map being linear in the number of measurements, which we previously stated to be true for a STM map (Section 5.3). To motivate this statement, we analyse the cost of inference by simulating two scenarios we expect a robot to frequently encounter in practice: incrementally observing new regions of the environment, and reobserving previously observed regions. It should be noted that to quantify the cost of inference, we count the number of outgoing messages calculated when updating

the map (Algorithm 1, lines 13 and 16). This is an appropriate metric as it measures the number of iterations for the inner-most loops of our inference algorithm.

For both scenarios, we represented the surface of the environment using a 2.5-D surface generated using Perlin noise¹⁸—a different surface was generated for each scenario. A single submap was used containing 1024 surfels. Simulated measurements were generated within the relative IRF of the submap by randomly sampling the surface in the observed region (we will discuss the sampling strategies further shortly), and then adding zero-mean non-identically distributed Gaussian noise to each sample. The noise covariance was determined by randomly rotation a diagonal covariance matrix. We also ensured that the measurement density in the observed region was approximately uniform and constant across all time-steps, at 10 measurements per surfel. Finally, after updating the map at each time-step, all the new measurements are windowed.

In the first scenario, we simulated a newly observed region of the environment shifts incrementally forward—this is typically the case for a robot driving with a 2-D LiDAR sensor mounted in a push-broom configuration. At each time-step, simulated measurements are generated from a sampling region (Figure 12a), and the map is updated with the new measurements. The cost of inference for this experiment is shown in (Figure 12b). We see that the total number of messages passed at each time-step has a linearly decreasing trend, which is expected due to the linearly decreasing sampling region. When we normalise the message counts in each update by the number of new measurements in the update, then this normalised message count is relatively constant. Note that with each incremental update only local regions of the map were significantly affected (Figure 12c).

In the second scenario, we simulated a region of the environment that is repeatedly observed. This emulates a robot revisiting a previously explored region, or a static robot repeatedly observing the same region. At each time-step, simulated measurements are generated by sampling from the entire mapping region. The number of messages passed follows an exponentially decreasing trend (Figure 13); that is, subsequent observations of a previously-observed region become computationally cheaper. This is because fewer iterations are required

From these two scenarios we see that updating a STM map does indeed have a linear computational cost in the number of measurements, which makes STM mapping a viable online dense mapping technique for the scenarios we expect a robot to encounter in a practical application. We have, however, only analysed the relative computational cost of performing inference on a STM map. When considering the absolute computational cost, one of most important aspects is the message and factor dimensionality. In our algorithm a message passed between neighbouring surfels has at most two dimensions, a message passed within a surfel has three dimensions, and the largest factor has six dimensions. These dimensions are all fixed and relatively low, therefore dimensionality is not a problem for our algorithm. Additionally, although our unoptimised Python implementation takes ± 3 ms per measurement to update a STM map¹⁹, with an efficient implementation we expect significantly faster results.

6.3. Model Accuracy Comparison

A STM map is an explicit surface representation that also captures model uncertainty. Therefore, to evaluate the modelling accuracy of a STM map, we compare it against a similar class of mapping techniques; namely, ones that use an explicit surface representation and capture model uncertainty. From our summary of the key attributes of the existing mapping techniques (Table 1), the suitable candidate mapping techniques are normal distributions transform (NDT) mapping, Gaussian process (GP) mapping, and elevation mapping. However, NDT mapping is not able to model measurement uncertainty, and GP mapping is intractable as an online dense mapping technique due to the cubic computational complexity. We therefore only compare STM mapping against standard elevation mapping—that is, each height is updated using a one-dimensional Kalman filter [15, 16].

¹⁸A type of gradient noise originally developed by Perlin [64], which is used to procedurally generate virtual environments and textures in computer graphics.

¹⁹This is based on an upcoming experiment (Section 6.5) using 19 million measurements.

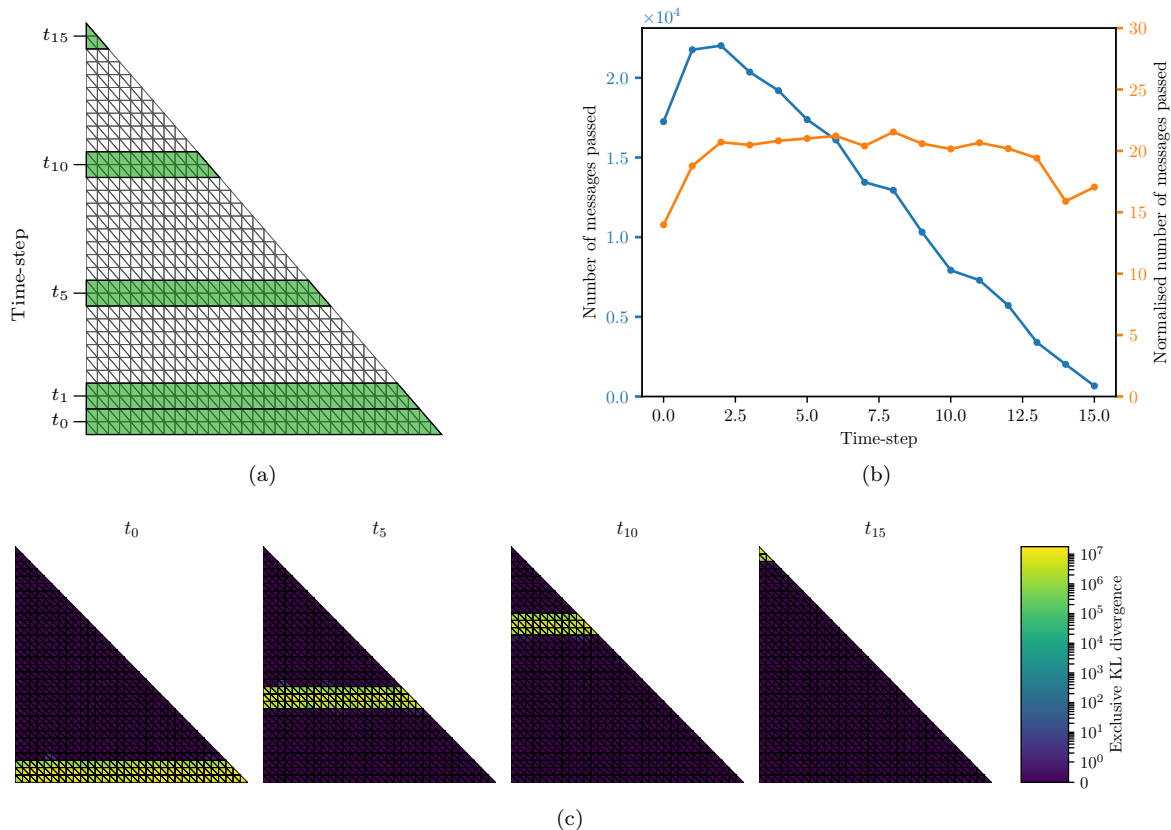


Figure 12: An experiment showing the cost of inference for the scenario where new regions of the environment are incrementally observed. (a) The experimental setup showing the sampling regions at selected time-steps (green, shaded). Note that the size of the sampling region at each time-step decreases linearly. (b) The cost of inference is quantified by the number of messages passed (blue, left axis). This message count is also normalised by the number of new measurements in each update (orange, right axis). (c) To visualise the incremental changes in the surfel beliefs we calculate the exclusive Kullback-Leibler (KL) divergence between the surfel beliefs before and after the measurements at a specific time-step have been incorporated. Note, the colour-mapping is scaled using a symmetrical logarithm, which is linear on $[0, 1]$ and logarithmic everywhere else.

We perform this comparison using simulated measurement data by quantifying each model’s accuracy against the ground truth using the mean squared error (MSE) of each model, and the log likelihood-ratio between both models. Using the same set of measurements, models were built for increasingly finer grid divisions. We first perform this comparison on a 2-D environment²⁰ as it is more intuitive to visualise, and we then extend this to a 3-D environment, which is generated using Perlin noise. We also ensured that there were ± 10 measurements per surfel at the finest grid division (for both the 2-D and 3-D experiments).

The results for the 2-D experiment are shown in Figure 14. The MSE of the STM map is better than that of the elevation map for all grid divisions greater than zero. When there is no subdivision (grid division depth = 0), because the average gradient of the surface of the environment is close to zero, the mean plane of the only surfel in the STM map is almost zero and at the same height as the elevation map (Figure 14c, grid division depth = 0). As the grid divisions increase past a certain point, the accuracy of both models begins

²⁰The 2-D simulation environment was created using the height profile of a mountain extracted using manual photogrammetry.

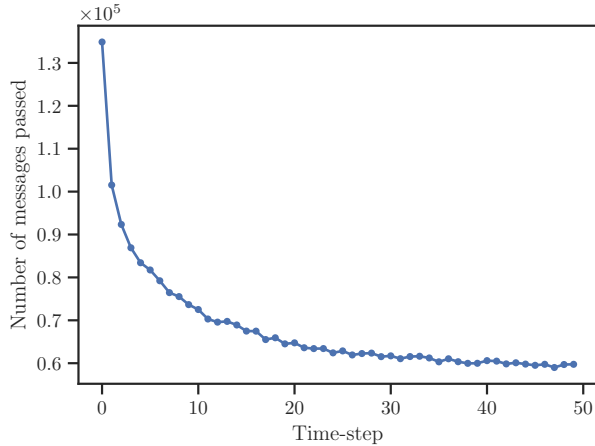
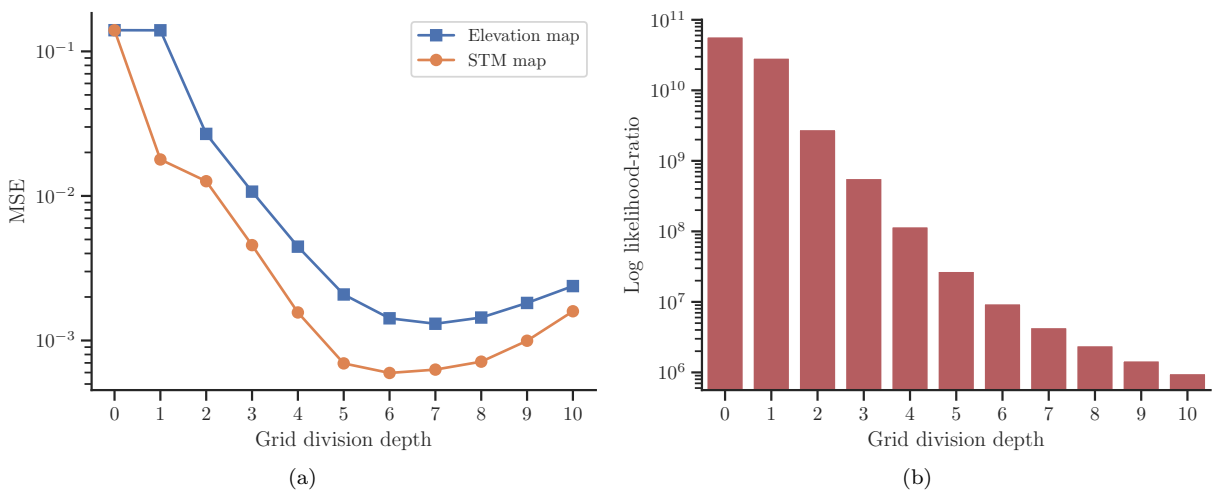


Figure 13: An experiment showing the cost of inference for the scenario where the same region of the environment is repeatedly observed.

to degrade (from the MSE this occurs for grid divisions > 6 for the STM map and > 7 for the elevation map). This effect is attributed to the measurement noise (relative to the size of the grid element) becoming too large, and the number of measurements in each grid element decreasing with each grid division. The effect is apparent when looking at the grid division depth of 8 in Figure 14c. From the MSE alone, this result might not appear significant; looking at log likelihood-ratio shows that for this environment, the STM map is a more likely model by orders of magnitude. This is as a consequence of the elevation map only estimating the mean height of the surface, whereas the STM map representing the surface as a stochastic process, which is a better representation of the surface of the environment.

For the 3-D experiment we ran a batch simulation for 10 synthetically generated environments (Figure 15). Compared to the 2-D experiment, we see a similar trend in the MSE, namely the STM map is clearly and consistently better than the elevation map for grid division greater than 2. Interestingly, as the grid divisions decrease, there is also a decrease in the batch MSE standard deviation for both models (> 2 grid divisions). This is because the lower grid divisions are too coarse to effectively represent the environment, and therefore the model accuracy is largely dependent on the particular generated environment. Similarly to the 2-D experiment, the log likelihood-ratio between both models shows that a STM map is a



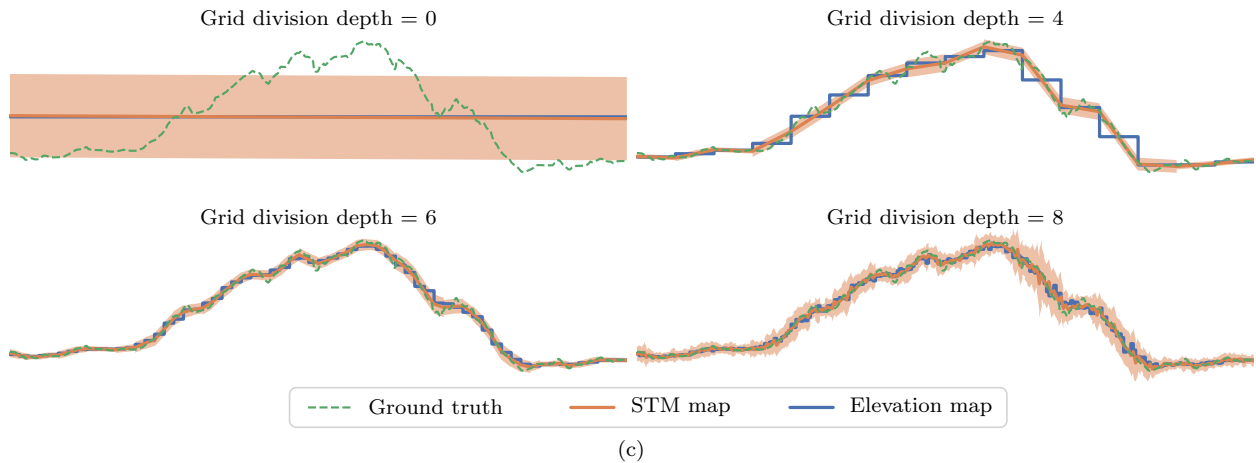


Figure 14: An experiment showing a 2-D simulation comparing a stochastic triangular mesh (STM) map with the standard elevation map [15, 16]. For increasing grid divisions we calculate (a) the mean squared error (MSE) of each method compared to the ground truth surface, and (b) the log likelihood-ratio between the STM map and the elevation map is evaluated along the ground truth surface; that is, $\log(\text{STM map likelihood}) - \log(\text{elevation map likelihood})$. Note that the vertical axis for both comparisons uses a log scale. (c) We also show the ground truth and resulting models for selected grid depths. The shaded regions indicate the one standard deviation confidence intervals in both models (the elevation map standard deviations are too small to be seen).

significantly better representation than an elevation map.

From these results, we can conclude that, in comparison to a standard elevation map, a STM map is a more accurate and a better representation of the environment for appropriately chosen grid divisions.

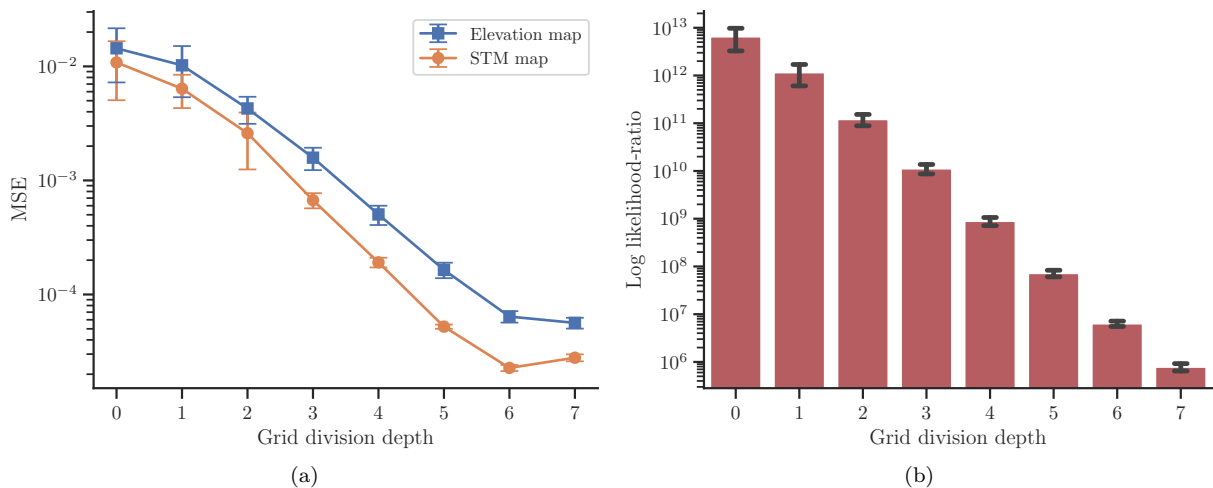


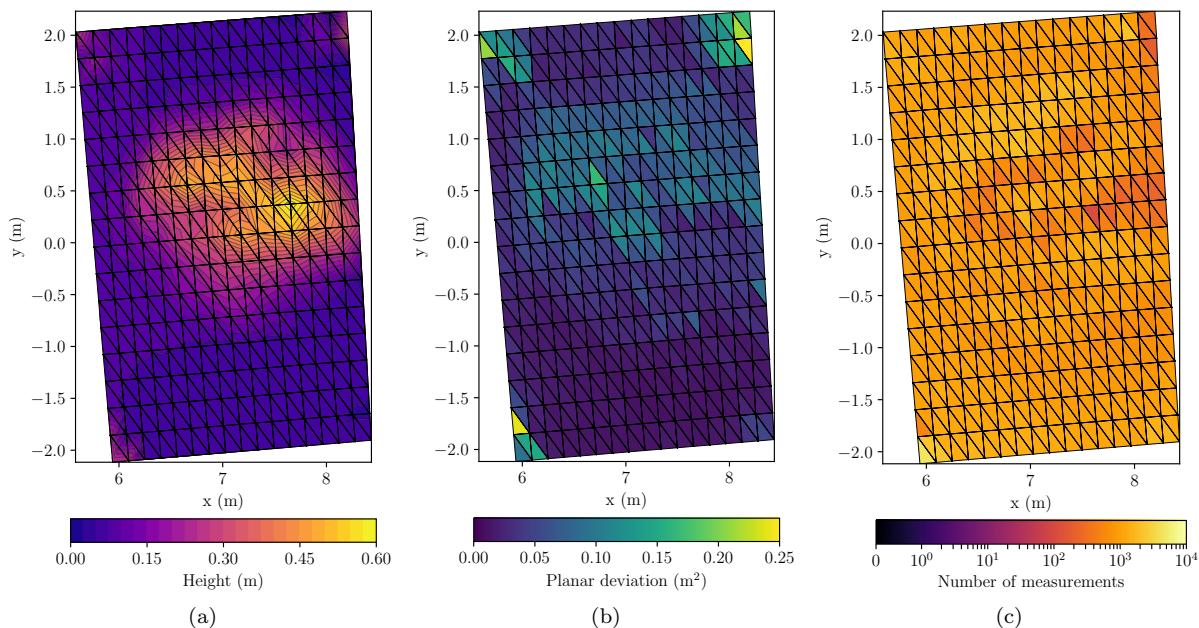
Figure 15: An experiment showing a 3-D batch simulation ($n = 10$) comparing a stochastic triangular mesh (STM) map with the standard elevation map [15, 16] for various generated environments. The mean and first standard deviation are shown for the (a) the mean squared error (MSE) of each method compared to the ground truth surface, and (b) the log likelihood-ratio between the STM map and the elevation map is evaluated along the ground truth surface; that is, $\log(\text{STM map likelihood}) - \log(\text{elevation map likelihood})$.

6.4. STM Mapping in a Relative IRF

Although robustly and persistently identifiable landmarks are not currently possible for general environments, there are still viable practical applications using landmark-based relative IRFs. In order to demonstrate this, we place artificial landmarks in the environment in the form of ArUco markers [65]—a popular open-source library enabling the creation and detection of binary square fiducial markers. Using these landmarks to define the submapping region, we are able to create a STM map using only three pairs of stereo images (Figure 16). The images were acquired using a stereo setup consisting of two 1.3 MP FLIR Flea3 GigE cameras at baseline of 18 cm. We calculated disparity maps (depth images) from image pairs using the library for efficient large-scale stereo matching (LIBELAS) by Geiger et al. [66]. The disparity maps were then transformed to noisy 3-D point measurements using the unscented transform [49]. Following this process, 525 331 point measurements were extracted from the three image pairs and incorporated into a STM map.

When considering the resulting STM maps, we see that the height maps are visually consistent with the environment. In the rougher regions of the environment (the gravel heap and landmarks in the corners) we see elevated planar deviations, whereas in the smooth regions (the asphalt path) the planar deviations are low. This illustrates the usefulness of the planar deviation in a STM map quantifying the surface roughness, which could be used as a measure of terrain drivability. Additionally, despite there being occlusions in the viewpoints (Figures 16g, 16k and 16o), the resulting height maps in these occluded regions are affected by the inference process, and are consistent with a smoothly varying environment. This is due to the correlated prior over the surfel vertex heights (Section 6.1). From this experiment, the resulting map beliefs show that a STM map that is visually consistent with the environment can be constructed from only a few viewpoints. This is also performed using stereo camera measurements, which have large range uncertainty.

This test simultaneously demonstrates the success of performing dense mapping in a relative IRF for two practical scenarios: the worst-case SLAM scenario, where there is no information about the robot motion; and the scenario where multiple robots are mapping the same region of the environment. From the perspective of the first scenario, this shows how using a relative IRF fits into the SLAM framework, and can handle performing dense mapping even without any pose information (except that which can be calculated from the landmarks). From the perspective of the second scenario, we illustrate the simplicity of using a relative IRF to perform multi-robot mapping. The maps created from each stereo image pair



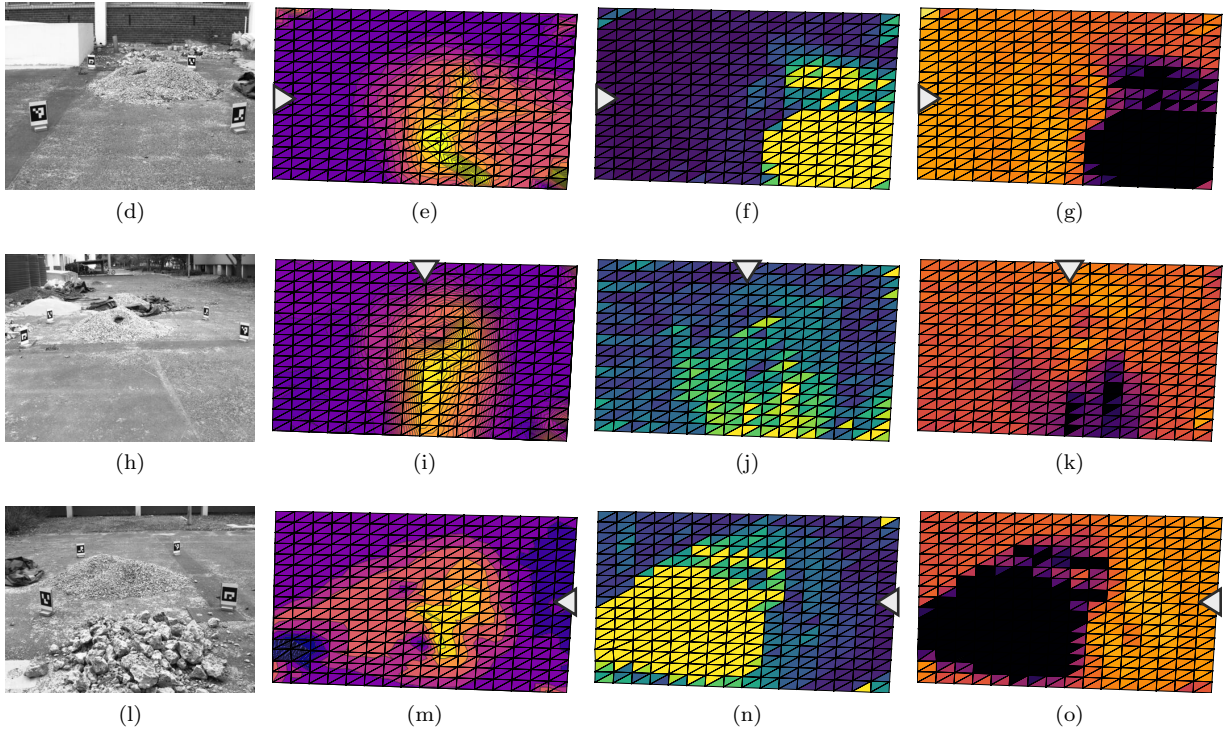


Figure 16: An experiment showing a STM map created using only three pairs of stereo images of an outdoor environment. This was possible by using relative IRFs to construct two submaps, with artificial ArUco markers [65] as landmarks. Each submap contains 256 surfels. The resulting map is shown for (a) the mean of the mean mesh belief, and (b) the planar deviation beliefs—calculated according to Equation (38). (c) We also show the number of measurements incorporated into each surfel on a symmetrical logarithmic scale, with a linear region on $[0, 1]$. (d-o) The STM maps built for each stereo image pair—namely, (d-g) a front view, (h-k) a side view, and (l-o) a rear view—is on the same scale as (a-c). The viewpoints are indicated using arrows. Notably, the occlusions are evident due to lack of measurements (g, k, o). The orientation of (a-c) is consistent with the front view (d)—that is, a 90° rotation of (e-g).

represent a robot’s perspective (Figures 16d to 16o). As each submap is created relative to the landmarks in the environment, the submaps are already aligned and can be fused together to form a single belief over the environment (Figures 16a to 16c).

6.5. STM Mapping in a Global IRF

In order to demonstrate the ability to use STM mapping in a global IRF, we use the Canadian planetary emulation terrain 3-D mapping dataset by Tong et al. [67]. Specifically, we use the `box_met` dataset²¹ taken in the Mars emulation terrain—a (60×120) m outdoor area. The `box_met` dataset consists of 19 044 655 LiDAR measurements, taken from 112 poses, and aligned using a differential global positioning system (DGPS).

In order to construct a STM map, a global IRF was created for the rectangular mapping region. The region was subdivided into two submaps, each containing 65 536 surfels. From the resulting STM map (Figure 17), we see that the mean mesh belief (Figure 17b) is visually consistent with satellite imagery. From the zoomed-in region (Figure 17d), we see that all the major features, even small rocks, visible in

²¹http://asrl.utias.utoronto.ca/datasets/3dmap/box_met.html

the satellite imagery of the environment are also visible in the map belief. We again see that the planar deviation beliefs (Figure 17c) are visually consistent with the terrain roughness. The steeper regions in the environment, which have a higher planar deviation, also form an outline of the obstacles in the environment. This experiment demonstrates that a STM map can be created in a global IRF framework. Although this forgoes the benefits of a relative IRF, the added complexity of a relative IRF may not be necessary in situations where the robot localisation is guaranteed to perform accurately; however, this is generally not the case. Additionally, this experiment shows that STM maps can handle datasets with a large number of measurements.

7. Conclusions and Future Work

To address the drawbacks in existing dense mapping techniques, we presented the stochastic triangular mesh (STM) mapping technique, which: represents the structure in the environment using a collection of stochastic processes, forming a continuous representation; is efficient to update, with approximately linear computation time in the number of measurements; is able to handle uncertainty in both measurements and the robot pose; and allows online operation by incrementally updating the map. Although existing techniques have some of these attributes, STM mapping is the only technique that is able to achieve them all. We have shown that a STM map is a more accurate and a better representation of the environment in comparison to the standard elevation map [15, 16], when evaluated in terms of mean squared error and model likelihood. Qualitative results on practical datasets showed that STM maps provide an accurate and descriptive model of the surface of the environment. Additionally, we showed that STM maps are agnostic to the sensor modality, and can handle both accurate (LiDAR) and inaccurate (stereo camera) sensors. Therefore, if a sensor can produce point measurements, it can be used with a STM map.

In addition to presenting the STM mapping technique, we have also demonstrated dense mapping using relative inertial reference frames (IRFs) in the hybrid metric map (HYMM) submapping framework [2, 3], and extended the framework to 3-D. Using this submapping approach decouples the process of localisation from that of dense mapping. The HYMM submapping framework complements the STM mapping technique, because it uses triangular submapping regions that seamlessly incorporates the triangular surfels in a STM map.

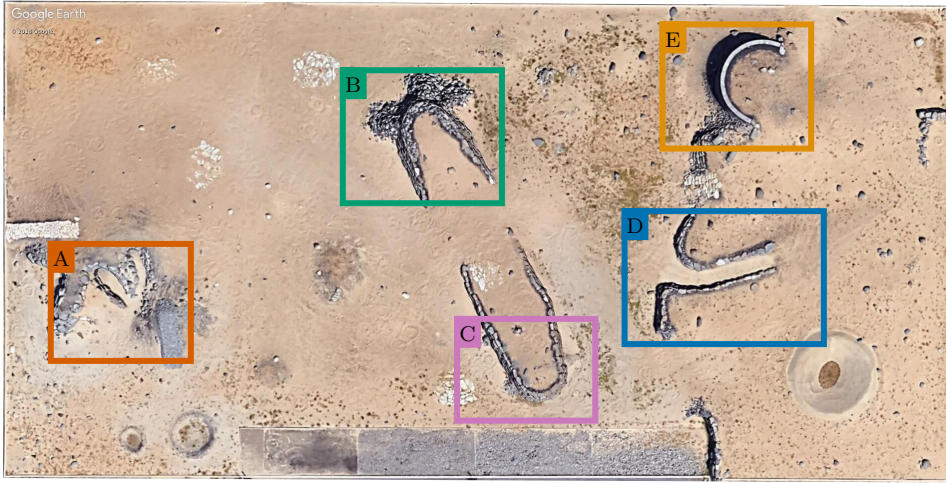
7.1. Future Work

The environment often consists of large homogeneous regions, and consequently naively dividing a dense map into fixed-sized elements is an inefficient use of storage. Therefore, in order for STM maps to better model the environment, future work will look at adaptively subdividing the grid. Surfels with very low planar deviations could be grouped into a coarser resolution, and conversely, surfels with high planar deviations could be subdivided into a finer resolution. This, however, would add complexity to the inference process. As most environments with practical significance are not static, it would be desirable to relax the static environment assumption. Future work will look at incorporating temporal information into the map to facilitate this. Additionally, as a motivation for STM maps is to be used in the context of autonomous navigation, future work will look at specialised planning algorithms to exploit the rich environment representation of a STM map.

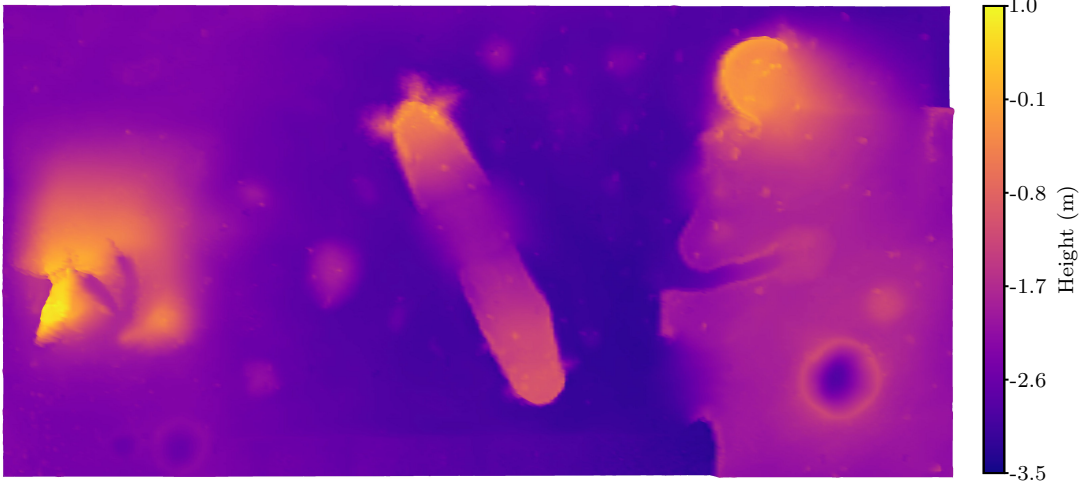
Acknowledgements

The authors would like to thank Johan du Preez for the valuable discussions, and allowing the use of the in-house probabilistic graphical modelling toolbox.

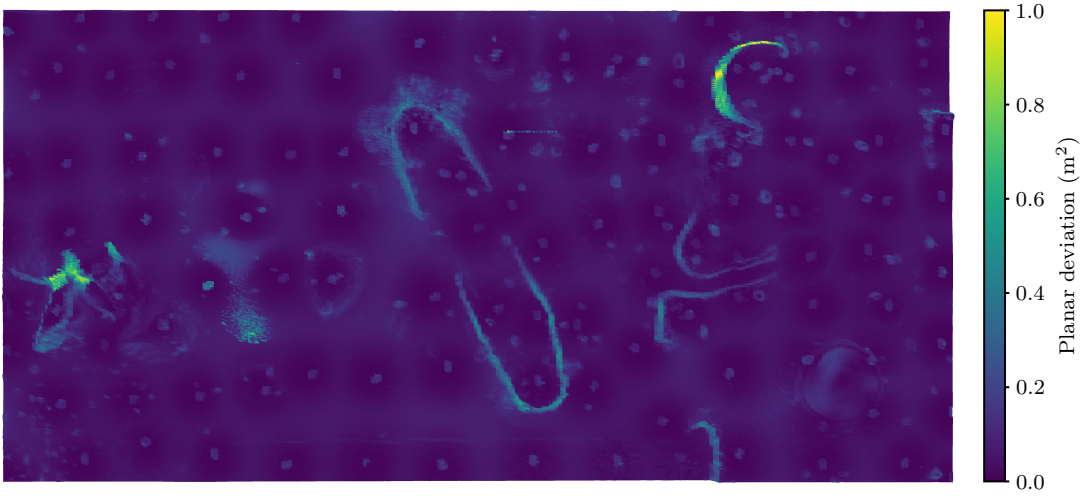
The financial assistance of the National Research Foundation (NRF) towards this research is hereby acknowledged. Opinions expressed and conclusions arrived at, are those of the authors and are not necessarily to be attributed to the NRF. The financial assistance of Armscor towards this research is hereby acknowledged.



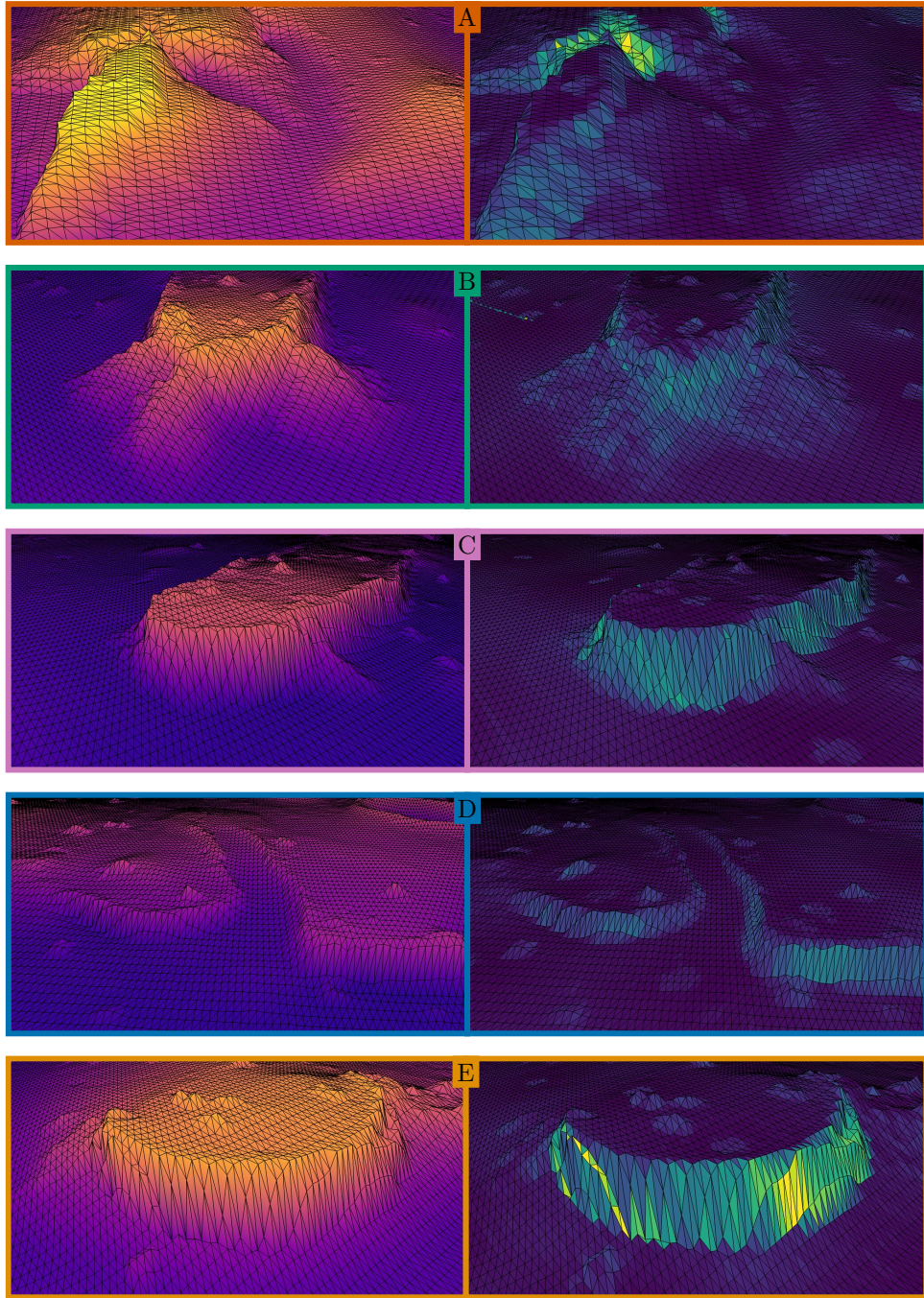
(a)



(b)



(c)



(d)

Figure 17: An experiment showing a STM map created in a global IRF using the Canadian planetary emulation terrain 3-D mapping dataset [67]. (a) A satellite view of the mapping region is shown (Google Earth). Note that five zoom regions are demarcated using coloured rectangles and labelled A-E. The resulting map is shown for (b) the mean of the mean mesh belief, and (c) the planar deviation beliefs—calculated according to Equation (38). (d) The map belief for the zoomed regions are shown, and share the same colour-maps as in (b, c).

References

- [1] V. Guizilini, F. Ramos, Towards real-time 3D continuous occupancy mapping using Hilbert maps, *The International Journal of Robotics Research* 37 (2018) 566–584. doi:10.1177/0278364918771476.
- [2] J. Guivant, E. Nebot, J. Nieto, F. Masson, Navigation and Mapping in Large Unstructured Environments, *The International Journal of Robotics Research* 23 (2004) 449–472. doi:10.1177/0278364904042203.
- [3] J. Nieto, J. Guivant, E. Nebot, DenseSLAM: Simultaneous Localization and Dense Mapping, *The International Journal of Robotics Research* 25 (2006) 711–744. doi:10.1177/0278364906067379.
- [4] S. Thrun, C. Martin, Y. Liu, D. Hahnel, R. Emery-Montemerlo, D. Chakrabarti, W. Burgard, A Real-Time Expectation-Maximization Algorithm for Acquiring Multiplanar Maps of Indoor Environments With Mobile Robots, *IEEE Transactions on Robotics and Automation* 20 (2004) 433–442. doi:10.1109/tra.2004.825520.
- [5] T. Wiemann, K. Lingemann, J. Hertzberg, Optimizing Triangle Mesh Reconstructions of Planar Environments, *IFAC-PapersOnLine* 49 (2016) 218–223. doi:10.1016/j.ifacol.2016.07.735.
- [6] J. Zienkiewicz, A. Tsiotsios, A. Davison, S. Leutenegger, Monocular, Real-Time Surface Reconstruction Using Dynamic Level of Detail, in: *2016 Fourth International Conference on 3D Vision (3DV)*, IEEE, 2016, pp. 37–46. doi:10.1109/3DV.2016.82.
- [7] H. Moravec, A. Elfes, High resolution maps from wide angle sonar, in: *IEEE International Conference on Robotics and Automation*, volume 2, Institute of Electrical and Electronics Engineers, 1985, pp. 116–121. doi:10.1109/ROBOT.1985.1087316.
- [8] A. Hornung, K. M. Wurm, M. Bennewitz, C. Stachniss, W. Burgard, OctoMap: an efficient probabilistic 3D mapping framework based on octrees, *Autonomous Robots* 34 (2013) 189–206. doi:10.1007/s10514-012-9321-0.
- [9] E. Einhorn, C. Schroter, H.-M. Gross, Finding the adequate resolution for grid mapping - Cell sizes locally adapting on-the-fly, in: *IEEE International Conference on Robotics and Automation*, IEEE, 2011, pp. 1843–1848. doi:10.1109/ICRA.2011.5980084.
- [10] S. Khan, D. Wollherr, M. Buss, Adaptive rectangular cuboids for 3D mapping, in: *IEEE International Conference on Robotics and Automation*, IEEE, 2015, pp. 2132–2139. doi:10.1109/ICRA.2015.7139480.
- [11] D. Droschel, M. Schwarz, S. Behnke, Continuous mapping and localization for autonomous navigation in rough terrain using a 3D laser scanner, *Robotics and Autonomous Systems* 88 (2017) 104–115. doi:10.1016/j.robot.2016.10.017.
- [12] D. Joubert, W. Brink, B. Herbst, Pose Uncertainty in Occupancy Grids through Monte Carlo Integration, *Journal of Intelligent & Robotic Systems* 77 (2015) 5–16. doi:10.1007/s10846-014-0093-y.
- [13] S. Thrun, Learning occupancy grid maps with forward sensor models, *Autonomous Robots* 15 (2003) 111–127. doi:10.1023/A:1025584807625.
- [14] M. Hebert, C. Caillas, E. Krotkov, I. Kweon, T. Kanade, Terrain mapping for a roving planetary explorer, *IEEE International Conference on Robotics and Automation* (1989) 997–1002. doi:10.1109/ROBOT.1989.100111.
- [15] R. Triebel, P. Pfaff, W. Burgard, Multi-level surface maps for outdoor terrain mapping and loop closing, in: *IEEE International Conference on Intelligent Robots and Systems*, IEEE, 2006, pp. 2276–2282. doi:10.1109/IR0S.2006.282632.
- [16] P. Fankhauser, M. Bloesch, M. Hutter, Probabilistic Terrain Mapping for Mobile Robots with Uncertain Localization, *IEEE Robotics and Automation Letters* 3 (2018) 3019–3026. doi:10.1109/LRA.2018.2849506.
- [17] T. K. Marks, A. Howard, M. Bajracharya, G. W. Cottrell, L. H. Matthies, Gamma-SLAM: Visual SLAM in unstructured environments using variance grid maps, *Journal of Field Robotics* 26 (2009) 26–51. doi:10.1002/rob.20273.
- [18] R. A. Newcombe, S. Izadi, O. Hilliges, D. Molyneaux, D. Kim, A. J. Davison, P. Kohli, J. Shotton, S. Hodges, A. Fitzgibbon, KinectFusion: Real-time dense surface mapping and tracking, in: *IEEE International Symposium on Mixed and Augmented Reality (ISMAR)*, 2011, pp. 127–136. doi:10.1109/ISMAR.2011.6092378.
- [19] T. Whelan, M. Kaess, H. Johannsson, M. Fallon, J. J. Leonard, J. McDonald, Real-time large-scale dense RGB-D SLAM with volumetric fusion, *The International Journal of Robotics Research* 34 (2015) 598–626. doi:10.1177/0278364914551008.
- [20] A. Dai, M. Nießner, M. Zollhöfer, S. Izadi, C. Theobalt, BundleFusion: Real-Time Globally Consistent 3D Reconstruction Using On-the-Fly Surface Reintegration, *ACM Transactions on Graphics* 36 (2017). doi:10.1145/3054739.
- [21] V. Dietrich, D. Chen, K. M. Wurm, G. v. Wichert, P. Ennen, Probabilistic multi-sensor fusion based on signed distance functions, in: *IEEE International Conference on Robotics and Automation*, IEEE, 2016. doi:10.1109/icra.2016.7487333.
- [22] P. Biber, W. Strasser, The normal distributions transform: a new approach to laser scan matching, in: *IEEE International Conference on Intelligent Robots and Systems*, volume 3, IEEE, 2003, pp. 2743–2748. doi:10.1109/IR0S.2003.1249285.
- [23] E. Takeuchi, T. Tsubouchi, A 3-D scan matching using improved 3-D normal distributions transform for mobile robotic mapping, in: *IEEE International Conference on Intelligent Robots and Systems*, IEEE, 2006, pp. 3068–3073. doi:10.1109/IR0S.2006.282246.
- [24] M. Magnusson, A. Lilienthal, T. Duckett, Scan Registration for Autonomous Mining Vehicles Using 3D-NDT, *Journal of Field Robotics* 24 (2007) 803–827. doi:10.1002/rob.
- [25] T. Stoyanov, M. Magnusson, A. J. Lilienthal, Comparative evaluation of the consistency of three-dimensional spatial representations used in autonomous robot navigation, *Journal of Field Robotics* 30 (2013) 216–236. doi:10.1002/rob.21446.
- [26] J. P. Saarinen, H. Andreasson, T. Stoyanov, A. J. Lilienthal, 3D normal distributions transform occupancy maps: An efficient representation for mapping in dynamic environments, *The International Journal of Robotics Research* 32 (2013) 1627–1644. doi:10.1177/0278364913499415.
- [27] C. E. Rasmussen, C. K. I. Williams, *Gaussian processes for machine learning*, MIT Press, 2006.
- [28] T. Lang, C. Plagemann, W. Burgard, Adaptive Non-Stationary Kernel Regression for Terrain Modeling, in: *Robotics: Science and Systems*, Robotics: Science and Systems Foundation, 2007. doi:10.15607/rss.2007.iii.011.
- [29] C. Plagemann, S. Mischke, S. Prentice, K. Kersting, N. Roy, W. Burgard, A Bayesian regression approach to terrain

- mapping and an application to legged robot locomotion, *Journal of Field Robotics* 26 (2009) 789–811. doi:10.1002/rob.20308.
- [30] S. Vasudevan, Data fusion with Gaussian processes, *Robotics and Autonomous Systems* 60 (2012) 1528–1544. doi:10.1016/j.robot.2012.08.006.
- [31] R. Hadsell, J. a. Bagnell, D. Huber, M. Hebert, Space-carving Kernels for Accurate Rough Terrain Estimation, *The International Journal of Robotics Research* 29 (2010) 981–996. doi:10.1177/0278364910369996.
- [32] S. T. O’Callaghan, F. T. Ramos, Gaussian process occupancy maps, *The International Journal of Robotics Research* 31 (2012) 42–62. doi:10.1177/0278364911421039.
- [33] M. G. Jadidi, J. V. Miro, G. Dissanayake, Warped gaussian processes occupancy mapping with uncertain inputs, *IEEE Robotics and Automation Letters* 2 (2017) 680–687. doi:10.1109/lra.2017.2651154.
- [34] V. Tresp, A Bayesian committee machine, *Neural Computation* 12 (2000) 2719–2741. doi:10.1162/089976600300014908.
- [35] S. Kim, J. Kim, Recursive Bayesian updates for occupancy mapping and surface reconstruction, in: *Proceedings of the Australasian Conference on Robotics and Automation*, 2014.
- [36] J. Wang, B. Englot, Fast, accurate Gaussian process occupancy maps via test-data octrees and nested Bayesian fusion, in: *IEEE International Conference on Robotics and Automation*, 2016, pp. 1003–1010. doi:10.1109/ICRA.2016.7487232.
- [37] F. Ramos, L. Ott, Hilbert maps: Scalable continuous occupancy mapping with stochastic gradient descent, *The International Journal of Robotics Research* 35 (2016) 1717–1730. doi:10.1177/0278364916684382.
- [38] K. Doherty, J. Wang, B. Englot, Probabilistic map fusion for fast, incremental occupancy mapping with 3D Hilbert maps, in: *IEEE International Conference on Robotics and Automation*, 2016, pp. 1011–1018. doi:10.1109/ICRA.2016.7487233.
- [39] G. Grisetti, C. Stachniss, W. Burgard, Improved Techniques for Grid Mapping With Rao-Blackwellized Particle Filters, *IEEE Transactions on Robotics* 23 (2007) 34–46. doi:10.1109/tro.2006.889486.
- [40] T. Jones, Tractable Conflict Risk Accumulation in Quadratic Space for Autonomous Vehicles, *Journal of Guidance, Control, and Dynamics* 29 (2006) 39–48. doi:10.2514/1.10515.
- [41] C. E. van Daalen, T. Jones, Fast conflict detection using probability flow, *Automatica* 45 (2009) 1903–1909. doi:10.1016/j.automatica.2009.04.010.
- [42] J. Engel, T. Schps, D. Cremers, LSD-SLAM: Large-scale direct monocular SLAM, in: *European Conference on Computer Vision*, Springer, 2014, pp. 834–849. doi:10.1007/978-3-319-10605-2_54.
- [43] R. Mur-Artal, J. D. Tardós, ORB-SLAM2: an Open-Source SLAM System for Monocular, Stereo and RGB-D Cameras, *IEEE Transactions on Robotics* 33 (2017) 1255–1262. doi:10.1109/TR0.2017.2705103.
- [44] S. Friedman, H. Pasula, D. Fox, Voronoi Random Fields: Extracting the Topological Structure of Indoor Environments via Place Labeling, in: *International Joint Conference on Artificial Intelligence*, Morgan Kaufmann Publishers Inc., 2007, pp. 2109–2114.
- [45] K. Konolige, E. Marder-Eppstein, B. Marthi, Navigation in hybrid metric-topological maps, in: *IEEE International Conference on Robotics and Automation*, IEEE, 2011, pp. 3041–3047. doi:10.1109/ICRA.2011.5980074.
- [46] P. Schmuck, S. A. Scherer, A. Zell, Hybrid Metric-Topological 3D Occupancy Grid Maps for Large-scale Mapping, *IFAC-PapersOnLine* 49 (2016) 230–235. doi:10.1016/j.ifacol.2016.07.738.
- [47] S. Lowry, N. Sunderhauf, P. Newman, J. J. Leonard, D. Cox, P. Corke, M. J. Milford, Visual Place Recognition: A Survey, *IEEE Transactions on Robotics* 32 (2016) 1–19. doi:10.1109/TR0.2015.2496823.
- [48] S. J. Julier, J. K. Uhlmann, New extension of the Kalman filter to nonlinear systems, in: *Signal Processing, Sensor Fusion, and Target Recognition VI*, SPIE, 1997. doi:10.1117/12.280797.
- [49] S. Julier, The scaled unscented transformation, in: *American Control Conference*, IEEE, 2002. doi:10.1109/acc.2002.1025369.
- [50] H. Durrant-Whyte, T. Bailey, Simultaneous localization and mapping: part I, *IEEE Robotics & Automation Magazine* 13 (2006) 99–110. doi:10.1109/MRA.2006.1638022.
- [51] M. Dissanayake, P. Newman, S. Clark, H. Durrant-Whyte, M. Csorba, A solution to the simultaneous localization and map building (SLAM) problem, *IEEE Transactions on Robotics and Automation* 17 (2001) 229–241. doi:10.1109/70.938381.
- [52] D. Koller, N. Friedman, *Probabilistic graphical models: principles and techniques*, MIT Press, 2009.
- [53] D. M. Blei, A. Kucukelbir, J. D. McAuliffe, Variational Inference: A Review for Statisticians, *Journal of the American Statistical Association* 112 (2017) 859–877. doi:10.1080/01621459.2017.1285773.
- [54] T. Minka, Divergence measures and message passing, Technical Report, Technical report, Microsoft Research, 2005.
- [55] J. Winn, C. M. Bishop, Variational Message Passing, *Journal of Machine Learning Research* 6 (2005) 661–694.
- [56] T. P. Minka, Expectation propagation for approximate Bayesian inference, in: *Uncertainty in Artificial Intelligence*, 2001, pp. 362–369.
- [57] L. K. Saul, M. I. Jordan, Exploiting Tractable Substructures in Intractable Networks, in: *Advances in Neural Information Processing Systems*, MIT Press, 1996, pp. 486–492.
- [58] C. M. Bishop, *Pattern recognition and machine learning*, Springer, 2006.
- [59] S. Thrun, W. Burgard, D. Fox, *Probabilistic robotics*, MIT Press, 2005.
- [60] B. J. Frey, D. J. C. MacKay, A revolution: Belief propagation in graphs with cycles, in: *Advances in Neural Information Processing Systems*, MIT Press, 1998, pp. 479–485.
- [61] P. Rusmevichientong, B. Van Roy, An analysis of belief propagation on the turbo decoding graph with Gaussian densities, *IEEE Transactions on Information Theory* 47 (2001) 745–765. doi:10.1109/18.910586.
- [62] Y. Weiss, W. T. Freeman, Correctness of Belief Propagation in Gaussian Graphical Models of Arbitrary Topology, *Neural Computation* 13 (2001) 2173–2200. doi:10.1162/089976601750541769.
- [63] Y. Qi, T. P. Minka, Window-based expectation propagation for adaptive signal detection in flat-fading channels, *IEEE Transactions on Wireless Communications* 6 (2007) 348–355. doi:10.1109/TWC.2007.05237.

- [64] K. Perlin, An image synthesizer, SIGGRAPH Computer Graphics 19 (1985) 287–296. doi:10.1145/325165.325247.
- [65] S. Garrido-Jurado, R. Muñoz-Salinas, F. J. Madrid-Cuevas, M. J. Marín-Jiménez, Automatic generation and detection of highly reliable fiducial markers under occlusion, Pattern Recognition 47 (2014) 2280–2292. doi:10.1016/j.patcog.2014.01.005.
- [66] A. Geiger, M. Roser, R. Urtasun, Efficient large-scale stereo matching, in: Asian Conference on Computer Vision, Springer, 2011, pp. 25–38. doi:10.1007/978-3-642-19315-6_3.
- [67] C. H. Tong, D. Gingras, K. Larose, T. D. Barfoot, rick Dupuis, The Canadian planetary emulation terrain 3D mapping dataset, The International Journal of Robotics Research 32 (2013) 389–395. doi:10.1177/0278364913478897.